

Review

Strategies and Outlook on Metal Matrix Composites Produced Using Laser Powder Bed Fusion: A Review

Min-Kyeom Kim [†], Yongjian Fang [†], Juwon Kim, Taehwan Kim, Yali Zhang, Wonsik Jeong and Jonghwan Suhr ^{*}

Department of Mechanical Engineering, Sungkyunkwan University, Suwon 440746, Republic of Korea; drapix@skku.edu (M.-K.K.); yjfang0507@g.skku.edu (Y.F.); wonsik0412@g.skku.edu (W.J.)

^{*} Correspondence: suhr@skku.edu; Tel.: +82-31-290-7290

[†] These authors contributed equally to this work.

Abstract: Particle-reinforced metal matrix composites (MMCs) produced using the laser powder bed fusion (LPBF) technique have gained considerable attention because of their distinct attributes and properties in comparison with conventional manufacturing methods. Nevertheless, significant challenges persist with LPBF-fabricated MMCs: more design parameters over commercially available alloys and several defects resulting from inappropriate process conditions. These challenges arise from the intricate interaction of material- and process-related phenomena, requiring a fundamental understanding of the LPBF process to elucidate the microstructural evolution and underlying mechanisms of strengthening. This paper provides a comprehensive overview of these intricate phenomena and mechanisms, aiming to mitigate the process-related defects and facilitate the design of MMCs with enhanced mechanical properties. The material processing approach was suggested, covering from material design and LPBF to postprocessing. Furthermore, the role of in situ heat treatment on the microstructure evolution of MMCs was clarified, and several novel, potential strengthening theories were discussed for the LPBF-fabricated MMCs. The suggested strategies to address the challenges and design high-performance MMCs will offer an opportunity to develop promising LPBF-fabricated MMCs, while overcoming the material limitations of LPBF.

Keywords: metal matrix composite; laser powder bed fusion; heat treatment; defects; microstructure; strengthening mechanism



Citation: Kim, M.-K.; Fang, Y.; Kim, J.; Kim, T.; Zhang, Y.; Jeong, W.; Suhr, J. Strategies and Outlook on Metal Matrix Composites Produced Using Laser Powder Bed Fusion: A Review. *Metals* **2023**, *13*, 1658. <https://doi.org/10.3390/met13101658>

Academic Editor: Manoj Gupta

Received: 11 September 2023

Revised: 26 September 2023

Accepted: 26 September 2023

Published: 27 September 2023



Copyright: © 2023 by the authors. Licensee MDPI, Basel, Switzerland. This article is an open access article distributed under the terms and conditions of the Creative Commons Attribution (CC BY) license (<https://creativecommons.org/licenses/by/4.0/>).

1. Introduction

Metal matrix composites (MMCs) are composite materials that employ alloys, as a matrix, and reinforcements, such as ceramics, carbon-based materials (carbon nanotubes, graphene, etc.) and other alloys (Mo, W, etc.) [1]. In the MMCs, iron (Fe), aluminum (Al), nickel (Ni), and titanium (Ti) alloys are generally used as the metal matrices because of their excellent properties: high strength/stiffness, wear resistance, hardness, thermal conductivity, electrical conductivity, etc. [2–5]. These matrix alloys encompass distinct attributes and properties, thereby leading various industries to seek diverse types of alloys that align with their specific requirements.

For instance, Fe alloys are widely used in various industries, including automotive, infrastructure, and construction [6,7]. This is because the steels exhibit favorable mechanical properties, formability, and weldability at a relatively economical cost [8]. Al alloys, showing a lightweight, high specific strength, thermal/electrical conductivity, and corrosion resistance, have gained substantial attraction in automotive, aerospace, construction, electric device, and thermal management applications [9,10]. Meanwhile, Ni alloys possess excellent corrosion resistance and mechanical properties under extreme environments [11]. Because of their properties, Ni alloys are mainly used in the industrial applications in which resistance to corrosion, heat, and wear are required (e.g., gas turbines, chemical-treated instruments, nuclear power plants, and marine and aerospace applications) [12]. Ti alloys

exhibit excellent specific strength, biocompatibility and excellent resistance to chemical corrosion and fatigue [13,14]. They are commonly used in automotive, aerospace, medical, marine, and other applications in which lightweight and high mechanical properties are essential despite their high price [15,16].

As the properties of MMCs are varied by the combination of various matrix alloys and reinforcements, the several reinforcements suitable for the matrix alloys have been explored to improve their mechanical properties [17–19]. For instance, multiwalled carbon nanotube (CNT)-reinforced magnesium (Mg) alloy composite (1 wt.%) exhibited an increase in modulus and hardness by 90% and 450%, respectively, in comparison with pure Mg alloy. Aluminum (Al)-exfoliated graphite nanoplatelets (xGnPs) (1 wt.%), IN625/SiC (5 wt.%), and Inconel (IN) 625/TiC (5 wt.%) demonstrated an enhancement in hardness, showing increases of approximately 200%, 130%, and 30%, respectively, compared to each pure matrix alloy [19–21]. However, agglomeration and poor compatibility of reinforcements within the matrix alloys may degrade the mechanical properties via structural defects attributed to the debonded reinforcements [22]. Therefore, an understanding of the composite materials is essential when designing the types and weight fraction of the reinforcements for each matrix alloy.

As the interest and demand for high-performance alloys are on the rise in industries, laser powder bed fusion (LPBF) has emerged as a material processing technique capable of producing intricate microstructures with multiple length scales [23,24]. As the LPBF technique uses a laser to selectively melt powders (Figure 1), the material undergoes repetitive and high heating/cooling cycles, resulting in a complex microstructure distinct from that of conventional manufacturing methods. The cellular microstructures, attainable through LPBF, provide exceptional properties with uncompromised tensile strength and ductility [25]. The multiscale microstructure arises from localized, iterative heating/cooling cycles that function similarly to an annealing heat treatment for the materials [26,27]. The rapid solidification rates and thermal gradients, inherent in LPBF, lead to finer microstructures and potentially altered phase ratios [28,29]. Consequently, LPBF-fabricated MMCs have been continuously studied to understand the mechanism of the microstructural evolution and, therefore, to design exceptional properties through a desirable combination of matrix and reinforcements [30–33].

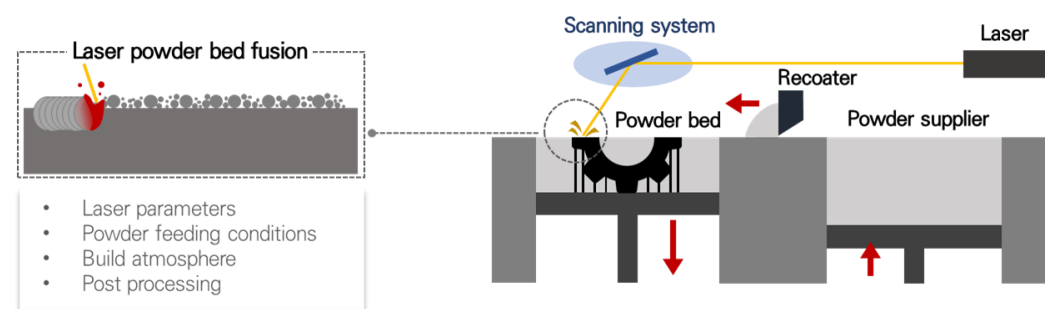


Figure 1. Schematics of the LPBF process and its related process parameters.

However, the fabrication of MMCs using LPBF requires meticulous work to optimize not only the composition ratio of the composite materials but also the LPBF process [34]. A lack of a comprehensive understanding of the material and process-related phenomena may lead to significant issues because of the many material- and process-related variables [35–37]. Given the localized heat source employed in the LPBF, the exquisite and iterative stacking process of the melt pools can give rise to defects, such as numerous pores and cracks, distortion, and delamination, under inappropriate conditions [38–41]. The formation of these defects is influenced by factors including the powder spreading, particle and melt pool dynamics, and the resultant deposited melt pools [42–46]. The factors are intricately linked to the material selection and process parameters, exerting a substantial impact on the quality of the LPBF-fabricated MMCs [47–50].

Initially, the quality of the spread powder layer is affected by the powder's morphology, size distribution, and recoating speed and layer thickness [45,51,52]. It is indispensable to carefully select and prepare the powders of the matrix alloy and reinforcements, taking into account the designed layer thickness in the LPBF. Subsequently, the precise control of the volumetric energy density (VED) is essential for manufacturing defect-free MMCs, which is achieved through the meticulous design of the laser and powder-related parameters. The VED is defined as follows [34]:

$$\text{VED} = \frac{\text{Laser power (P)}}{\text{Scan speed (v)} \times \text{Line spacing (h)} \times \text{Layer thickness (t)}} \quad (1)$$

A high energy density can lead to a substantial amount of spattering, large denudation zone, residual stress, and keyholing during the LPBF process [53–58]. These phenomena incur an increase in the surface roughness, the risk of pore and crack formation, distortion, and process failure [39,40]. Conversely, a low energy density can result in a balling, lack of fusion defects, and resultant delamination [56]. The insufficient melting of powders give rise to the unstable melt pools and inter-bead pores during the process [38,58]. To effectively suppress these defects, a comprehensive strategy to manufacture MMCs is required, which involves the systematic design of the individual inputs based on an in-depth understanding of the intricate phenomena.

During the LPBF process, the repetitive and rapid cycles of melting and solidification produce inhomogeneous and anisotropic microstructures [59–61]. A majority of grains elongate along the direction of heat dissipation, which is attributed to the severe temperature gradients and rapid solidification [62,63]. This occurs because these steep gradients dictate the direction of heat transfer and resultant solidification, and the severe temperature gradient inhibits the formation of equiaxed grains, which typically develop during both the low-temperature gradient and high solidification rate [64,65]. Consequently, the LPBF parts with columnar grains demonstrate that the properties are both anisotropic and inhomogeneous, distinct from those in traditionally manufactured alloys [60,66]. Thus, post-heat treatment emerges as a viable strategy to alleviate not only anisotropy but also residual stress through processes such as recrystallization and stress relief [67,68]. Notably, the as-built microstructures highly rely on multiple factors, including material type, machine setting, and process conditions [69–73]. To achieve the desired properties, it is necessary to reduce defects and understand both the as-built and heat-treated microstructures based on knowledge of the underlying strengthening mechanisms.

The control of qualities and enhanced properties, acceptable for engineering applications, are the main concerns in the LPBF-fabricated MMCs. However, a lack of material processing knowledge and a printing database used to incur significant problems in the LPBF process [37]. Despite existing studies on the challenges, comprehensive and in-depth reviews capable of providing holistic insight into both the material processing and strengthening mechanisms remain lacking [74]. This review paper offers a profound understanding of both the material processing and strengthening mechanisms, covering the various types of LPBF-fabricated MMCs. Furthermore, to evade trial-and-error efforts, the systematic strategies to design composite materials, LPBF process, and postprocessing were suggested to attain the desirable qualities and excellent properties. The extensive insight and strategies discussed here offer valuable guidance for manufacturing various types of LPBF-fabricated MMCs, which exhibit defect-free and excellent properties.

2. Strategies for Material-to-Process Design

2.1. Considerations in Material Design

2.1.1. Morphology of Powders

The LPBF technique typically demands spherical powders within the size range of 15 to 53 μm . The layer thickness is customarily set within the range of 15–100 μm , depending on both the powder's characteristics and laser spot size [75–79].

Nevertheless, nonspherical powders offer potential benefits in terms of the time and cost efficiency (Figure 2). However, their utilization can lead to flow instability and powder agglomeration, both of which can contribute to defect formation [80,81]. These issues stem from the significant influence of the powder's morphology and size on both the quality of the powder spread and packing density [82,83]. Consequently, employing nonspherical powders in LPBF requires additional spreading time to attain an appropriate spread quality, thus decreasing productivity.

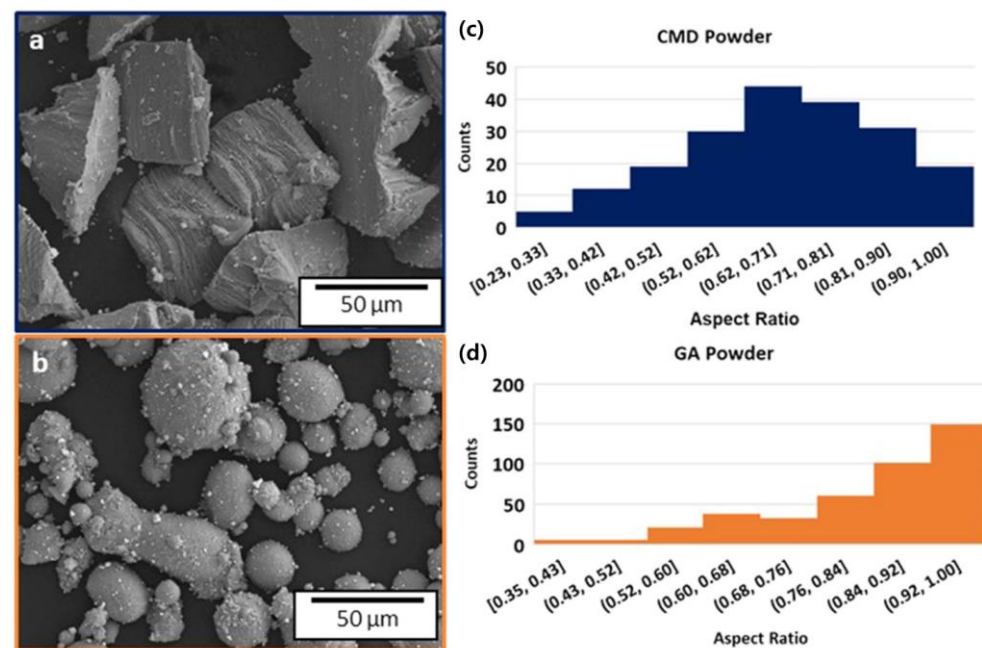


Figure 2. Morphology of (a) nonspherical and (b) spherical powders of Al7075 alloy produced using cold mechanically derived (CMD) and gas atomized (GA) techniques, respectively. Aspect ratio of (c) CMD and (d) GA powders [51].

The quality and uniformity of the powder layer play crucial roles in the defect formation due to the inadequate laser–material interaction and improper filling of melt pools [84,85]. These phenomena involve issues such as insufficient melting, balling, and humping during the LPBF process [86]. Furthermore, nonspherical powders can oxidize more easily compared to the spherical powders owing to their larger surface area and irregular, low packing density [87].

As a result, adopting powders with complex shapes such as fibers, flakes, plates, or whiskers may require more intensive efforts to optimize the LPBF process, thereby increasing the risk of quality degradation in LPBF products [88]. To address this, this paper proposes the manufacturing of MMCs, reinforced with the nano-to-micron sized particles, as an alternative to fiber, plate, or whisker-shaped reinforcements.

2.1.2. Types of Reinforcement and Their Compatibility with Matrix

In material design, a variety of reinforcements are employed to enhance the properties of LPBF-fabricated MMCs. The commonly used reinforcements include ceramic and metallic particles, as well as other nonspherical particles, such as metallic and ceramic fibers, carbon-based reinforcements (carbon fiber, (MW)CNT, and graphene), and whiskers [89–97]. The types of ceramic particles, widely employed in LPBF-fabricated MMCs, include SiC, SiO₂, Si₃N₄, Al₂O₃, AlN, B₄C, TiO₂, TiC, TiB₂, and ZrO₂ [89,94,98–110]. In the case of metallic particles, W, Mo, Ti, Ni, Cu, Co, Al, Fe, Mg, etc., are generally reinforced to improve properties or address issues in LPBF [111–114]. Ceramic particles tend to exhibit harder and more brittle properties of MMCs in comparison with their metal counterparts [107,108,115,116]. They can provide excellent attributes, such as wear resis-

tance, corrosion resistance, high-temperature stability, weight reduction, and lower thermal expansion coefficient, compared to metal reinforcements [117–121]. However, employing ceramic particles instead of metals may entail trade-off drawbacks, such as relatively low ductility and toughness, and thermal conductivity [122,123].

Among reinforcements, compatibility between the metal alloy matrix and the reinforcements is a major consideration in material selection for achieving robust interfacial bonding within MMCs [124]. Poor compatibility between the matrices and reinforcements can lead to separation during manufacturing or deterioration in the properties (Figure 3) [125]. To achieve the desirable compatibility, wettability of reinforcements, property mismatch and chemical reaction between them should be previously understood and considered when designing MMCs.

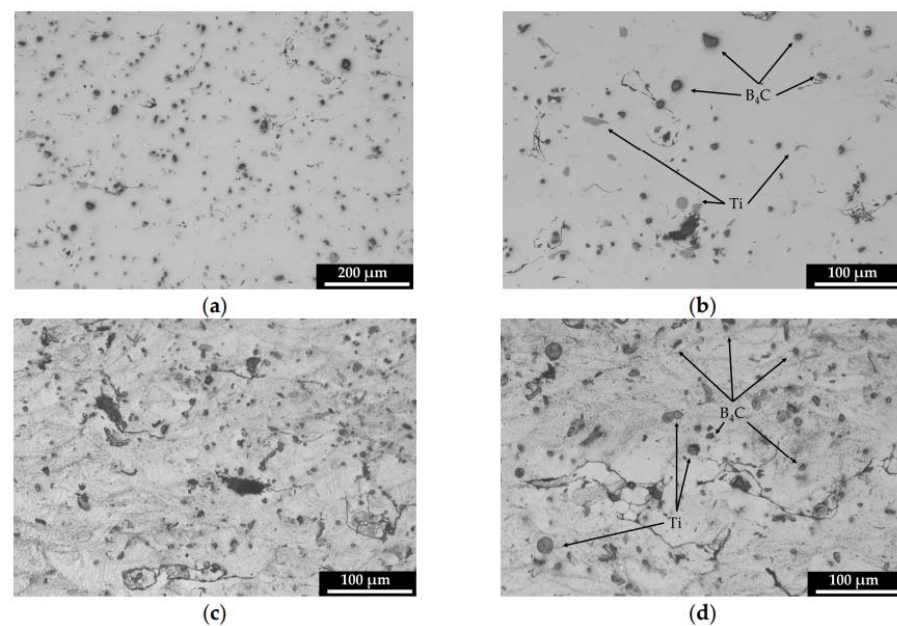


Figure 3. Optical micrographic images of A6061/Ti (2.5 wt.%) / B₄C (0.9 wt.%) at (a) lower and (b–d) higher magnifications, indicating microcracks, B₄C particle detachment, and unmelted particles [125].

A favorable wettability of the reinforcements is a prerequisite to attaining excellent bonding. For the interface between particles and the metal matrix, it plays an important role in the mechanical properties of particle-reinforced MMCs. During the deformation process of MMCs, the failure of the interface was found due to the high stress concentration at the poles of the particles [126,127]. Furthermore, during solidification, the appearance of a hydrostatic tensile stress field had the ability to deflect microcracks towards interfaces with cooling of MMCs, which was attributed to the difference in the thermal expansion coefficient between reinforced particles and the metal matrix [126,128]. Accordingly, it can be concluded that the mechanical properties of LPBF-fabricated particulate-reinforced MMCs will be affected by the characteristics of interfaces.

Additionally, the chemical reaction between the matrix and reinforcements is another concern when manufacturing MMCs [129]. The reaction can incur the formation of compounds during melting and solidification, thereby generating intermetallic compounds, oxide layers, interdiffusion zones, and other compounds at the interface under high temperature [130]. At elevated temperatures, atoms from the matrix and reinforcement materials can diffuse into each other, resulting in the formation of diffusion layers or interdiffusion zones at the interface [130]. The chemical compounds around the interface between the matrix and reinforcements can influence the mechanical properties of MMCs, which is discussed in more detail in Section 3.1.2 [131].

Low mismatch in the thermomechanical property is a critical aspect in avoiding premature failure of MMCs under applied loads. A considerable mismatch in the modulus

may facilitate the debonding between the matrix and the reinforcements, thereby potentially inducing the crack initiation from the debonded interface [22]. Furthermore, a substantial mismatch in the thermal expansion coefficient can deteriorate the interfacial bonding between them, which is attributed to the increase in residual stress [105]. To address the compatibility issues, employing coatings or investigating appropriate reinforcements for the matrix can emerge as strategic solutions.

2.1.3. Size Distribution of the Reinforcement

When reinforcements are incorporated into a matrix alloy, the size of the reinforcements can significantly affect the microstructural evolution during the LPBF process, as well as the resulting properties [98,132]. Generally, the inclusion of nanoparticles within the matrix alloy is more challenging than the microparticles. This is attributed to the nanoparticles' high surface energy, which can lead to several defects, such as particle agglomeration, increased residual stress, and cracking [133]. Nonetheless, the nanoparticles can enhance the mechanical properties more effectively than the microparticles [126]. The strengthening mechanism between nanosized and micron-sized particles typically differ due to their distinct interactions with the matrix alloy [114,134–139].

The nanoparticles produce refined grains and modified grain boundaries during the LPBF processing and heat treatment [135]. The nanoparticles can serve as nucleation sites during the solidification, increasing the number of nucleation sites and thus promoting the formation of refined grains [136]. Moreover, the nanoparticles can prevent grains from growing during the heat treatment by inhibiting their movement [137]. The inclusion of nanoparticles also alters the atomic structure and chemical compositions at grain boundaries, thus enhancing the strength, ductility, corrosion, and/or creep resistance [114,135,137,140]. In contrast, microparticles might have a less pronounced influence on the grain structures and grain boundary characteristics, offering less resistance to grain growth and dislocation movement during solidification [141].

The refined microstructures of nano-MMCs, combined with a high surface area-to-volume ratio of the nanoparticles, enable to hinder dislocation motion more effectively because of the enhanced interface interactions [142]. Therefore, the predominant strengthening mechanisms in the nano-MMCs involve the grain boundary, dispersion strengthening, etc. [143]. Meanwhile, the strengthening in the micro-MMCs is primarily based on load transfer mechanisms, such as particle/matrix interlocking and dislocation interactions [138,139]. The phenomena in the micro-MMCs enhance the mechanical, electrical, and thermal properties to a lesser extent compared to the nano-MMCs. Therefore, the nanosized and micron-sized reinforcements should be carefully selected to achieve the desired properties and processing for the specific applications.

2.1.4. Volume Fraction of Reinforcement

Higher volume fractions generally lead to enhanced mechanical properties and improved performance in areas such as strength, stiffness, and wear resistance [144,145]. However, increasing the volume fraction of reinforcements can also lead to challenges in achieving uniform dispersion and effective bonding between the reinforcement and matrix [146]. If the reinforcements agglomerate together forming clusters, the cracks easily nucleate and propagate due to the stress concentration and poor bonding between them [147]. On the other hand, a lower volume fraction of reinforcements may not achieve the desirable properties without significant improvement [148]. Therefore, the desirable volume fraction of reinforcements should be experimentally explored to avoid the defects and resultant property degradation. Additionally, as the requirements of properties depend on the standard of application, the specific volume fraction to attain the required properties need to be optimized, finding the optimum balance between the properties and processability.

2.2. LPBF Processing

2.2.1. Powder Preparation

The repeatability of the qualities and properties has been a major issue in the LPBF technique, because minor inconsistencies can significantly affect the safety and reliability of parts for critical applications [149]. Process-related physical metallurgical phenomena are highly sensitive to both process parameters and powders [150]. Thus, the LPBF technique needs meticulous machine calibration and quality control by regulating the situational variables associated with process inputs and powder conditions [54,151–153].

In preparing the powders for the LPBF, powder characteristics can potentially change based on the number of recycling cycles and the moisture content of the powders [154,155]. As powder recycling is indispensable for the LPBF because of its high cost, a strategy to use the recycled powders should be established, grounded in metallurgical insight. Repeated recycling can alter the powder's size distribution and chemical composition over time [156–158]. The powders, once exposed to a laser heat source, as well as the spatter, might have a nonspherical morphology after the LPBF, resulting in particle agglomeration and, subsequently, reduced spread quality [159,160]. Furthermore, contaminants on the powders and oxidation can change the chemical composition of as-built parts, potentially diminishing their strength or ductility [157].

Another pivotal aspect of powder preparation is the moisture content. The water molecules in humid powders can adversely impact the chemical reaction between shielding gas and the powder alloys during the processing (Figure 4) [161]. The moisture can interact with the alloys during the process, potentially generating oxides, hydroxides, or other unwanted impurities [162,163]. Moreover, the moisture can diminish powder flowability during spreading and reduce laser absorption due to water evaporation [154]. Such phenomena can lower the relative density of as-built parts, leading to degradation of their properties. Hence, strategies to manage recycled powder, taking into account their moisture content, should be established based on a thorough material processing knowledge.

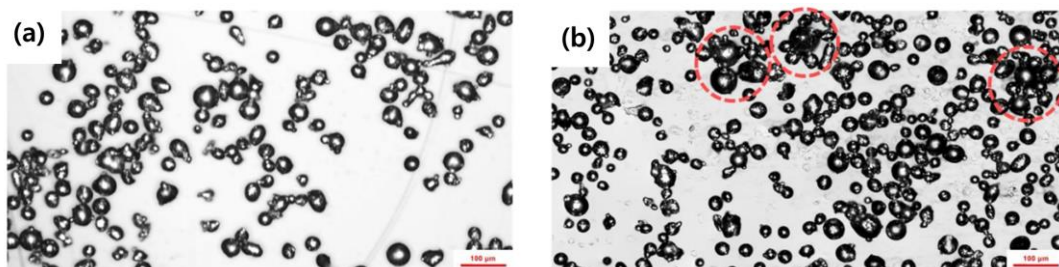


Figure 4. Optical microscopic images showing the powder spread quality: (a) dry powder (3.4%RH); (b) humid powder (60.0%RH). Red dashed circles indicate the particle agglomeration [161].

2.2.2. Process Atmosphere

The types and content of shielding gas play crucial roles in determining the reaction of the melt pool with the environment and the subsequent oxidation of the solidified alloy in the LPBF process [164–166]. Among the various shielding gases available for welding, Ar and N₂ gas are the most employed in the LPBF [167,168]. Ar with heavy atomic weight effectively prevent oxidation and contamination, making it suitable for processing reactive alloys, such as Ti and Al [168,169]. Meanwhile, N₂ gas is more typically selected for the less-reactive alloys, such as stainless steels and Ni alloys [165,170]. The N₂ gas employed in the LPBF may produce nitrogen-based compounds in as-built microstructures, which can improve corrosion resistance and alter mechanical properties [171–173]. Therefore, shielding gases must be carefully selected based on their application.

Furthermore, an insufficient amount of the shielding gas increases the evaporating pressure within the interaction zone of a laser-melt pool, thus inducing increased spattering and surface roughness [174,175]. These effects reduce the relative density and the resulting

mechanical properties of as-built parts [175,176]. Therefore, it is imperative to maintain a high level of shielding gas and ensure a minimal presence of oxygen throughout the LPBF process.

2.2.3. Process Parameters

In the LPBF process, various parameters concerning the spreading and melting of powders serve as sensitive inputs that determine the as-built qualities of MMCs. The process parameters, denoted by Equation (1), include laser power, scan speed, line spacing, and layer thickness. If the VED increases due to a higher energy input on a smaller melting volume, both the temperature and evaporation rate of the melt pool will significantly escalate, thereby enlarging its size and altering its morphology to a keyhole mode [54]. This melt pool behavior may generate keyhole-induced pores during the LPBF process (Figure 5) [34]. Conversely, a low VED can induce insufficient melting and lead to lack-of-fusion defects during the LPBF process [34]. These phenomena underscore the difficulty in controlling the parameters, owing to the complex metallurgical interactions occurring during the LPBF process [42,53,55].

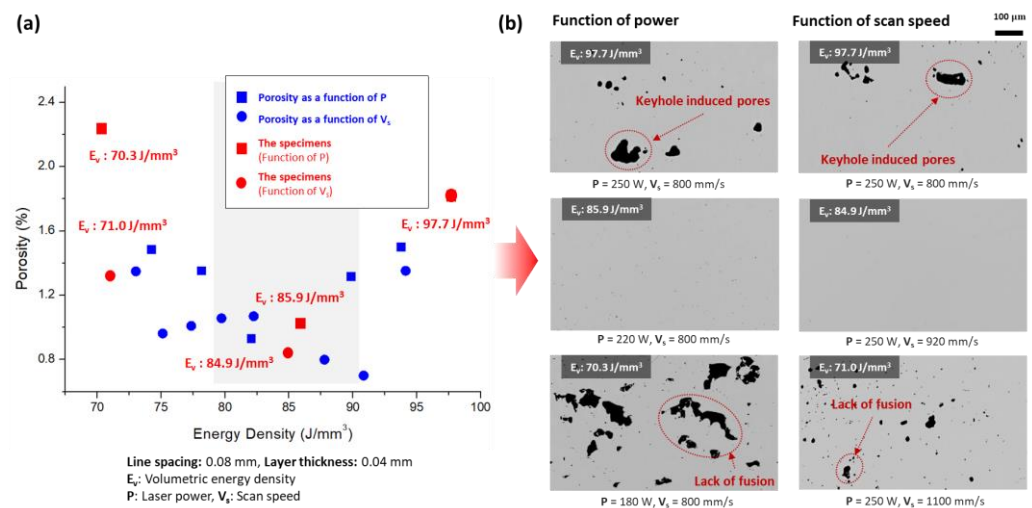


Figure 5. (a) Porosity and (b) optical microscopic images of pores in LPBF parts as a function of the volumetric energy density [34].

Consequently, most studies utilize VED as a tool for exploring feasible parameters, because it enables a reduction in the number of variables while ensuring part quality more readily [177]. However, it is worth noting that the energy absorption rate can vary, even under identical VED conditions, resulting in different melt pool dynamics and particle behaviors [54]. Furthermore, when incorporating reinforcements within a matrix alloy, MMCs must be additively manufactured with parameters that differ from those used for the matrix alloy alone [21,178]. The optimum parameters are highly contingent not only on the machine specifications but also on the powder conditions. As such, the current design approach has distinct limitations in achieving and consistently maintaining defect-free quality across various types of as-built MMCs for industrial applications.

Therefore, this paper proposes a systematic design approach for the LPBF process for MMCs, as detailed below. (1) Layer thickness should be set based on the size of the powder alloys employed for the LPBF. A larger layer thickness can promote productivity, increasing the surface roughness and decreasing the relative density and properties [179,180]. Conversely, a smaller layer thickness may damage the recoating surface and deteriorate the powder spread quality [79]. As the real layer thickness, called the effective layer thickness, is larger than the designed thickness [79], it is recommended to set the layer thickness just below the maximum size of the powder alloys. (2) The sizes and morphology of the melt pools of the MMCs should be characterized post-LPBF process completion. Although in

situ monitoring of melt pool behaviors is more accurate in the prediction and mitigation of defects, it is far from a cost-effective work. Therefore, ex situ characterization of melt pools should be performed to mitigate the defects, including lack-of-fusion and keyholing based on the reported printability map (Figure 6) [47,152,181]. (3) Optimum line spacing for the MMCs should be explored after determining the feasible layer thickness, laser power, and scan speed. This task can be performed through the measurement of the relative density in the as-built parts, manufactured with various line spacing values. (4) Nondestructive measurement and mechanical testing of the MMC parts, fabricated with the optimum parameters, can ensure structural integrity for industrial applications. This procedure requires intensive efforts due to the numerous tests and measurements required for each MMC. Therefore, a comprehensive printing database and materials processing knowledge are essential for further progress in the LPBF-fabricated MMCs.

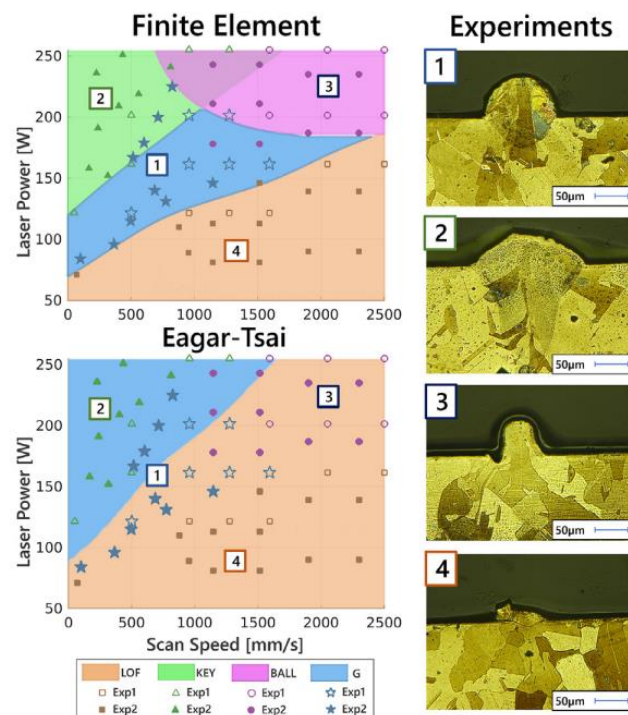


Figure 6. Printability maps that predict melt pool morphology regions for a Ni-5wt.%Nb alloy, depicted by good quality (blue, G), keyholing (green, KEY), balling (purple, BALL), and lack of fusion (orange, LOF) [47]. The numbers 1–4 correspond to the four optical images.

2.3. Postprocessing

After the LPBF process, as-built MMCs often do not meet the desired standards of quality, exhibiting high surface roughness, residual stress, and anisotropic properties [177,182]. Therefore, postprocessing, such as heat treatments and surface finishing, becomes indispensable to attain the requisite qualities for engineering applications [34,183]. The postprocessing involves a series of steps to enhance the qualities and properties of LPBF-fabricated MMCs, which are outlined as follows:

- (1) After the LPBF process, the as-built products and supports should be detached from a baseplate using a wire electrical discharge machining (EDM) or the other mechanical cutting processes.
- (2) Various heat treatments, such as hot isostatic pressing, solution, aging, and stress relief heat treatment, can be conducted depending on the requirements in the application [184–186]. During the LPBF process, the intended phases may not be obtained due to the fast-cooling rate and complex temperature history. Thus, the heat treatments can be applied to form the desirable phases [185]. Among the heat treatments, hot isostatic pressing stands out as an effective method to minimize defects in the

as-built parts by applying high pressure and temperature (Figure 7) [34,187]. Solution heat treatment, generally conducted for the precipitation-hardening alloys, allows for certain constituents to be dissolved into a single-phase solid solution [184]. When applied to Al alloys, this treatment enables dissolved precipitates to foster a uniform microstructure, enhancing the effectiveness of subsequent aging heat treatment [188]. This dissolution arises because of the high temperature and sufficient holding time, along with a rapid cooling rate. Aging heat treatment, also known as precipitation hardening, aims to produce precipitates in the solution-treated alloy under a low temperature over an extended period of time (Figure 8) [186]. Consequently, numerous precipitates or second-phase particles within the matrix can impede dislocation movement, thereby improving the mechanical properties after the aging heat treatment [189]. Stress relief heat treatment helps to secure the durability and structural integrity of as-built parts. This treatment relieves the internal residual stress below the lower transformation temperature during slow cooling period [188].

- (3) Machining and surface finishing are essential to attain acceptable levels of geometrical tolerance and surface roughness. Compared to engineering requirements, the as-built dimensional accuracy and roughness are unsatisfied due to the distortion and the inherent characteristics of the melt pool stacking process [182]. Therefore, surface finishing, such as laser polishing, finish machining, and vibratory surface finish, are frequently employed to address these issues.

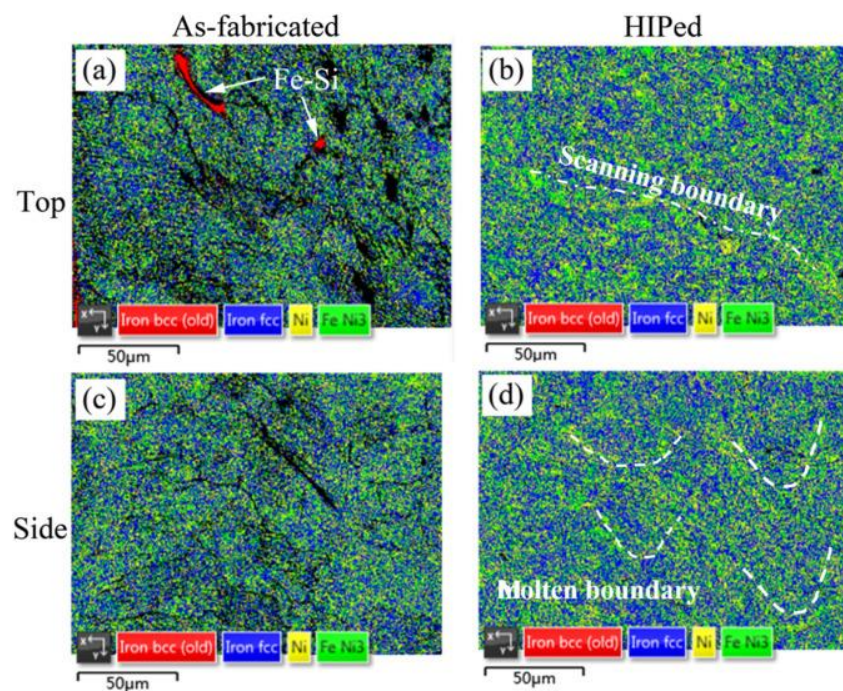


Figure 7. Phase distributional maps of LPBF-fabricated Fe–Ni–Si alloys (a,c) before and (b,d) after hot isostatic pressing from top and side views [187].

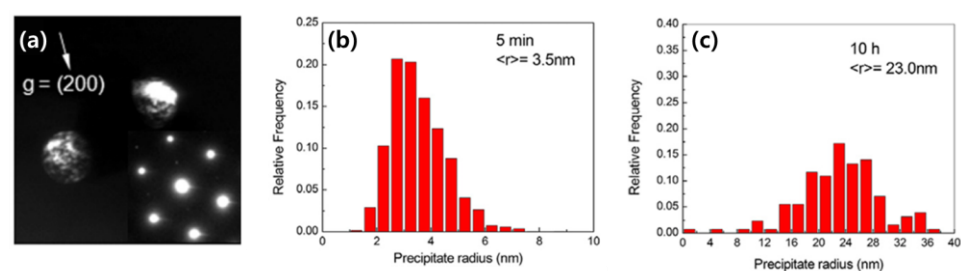


Figure 8. (a) Dark-field TEM images of precipitates and (b,c) precipitate size distributions in Al–B₄C composites aged at 450 °C for 5 min and 10 h [189].

The outlined procedure for the postprocessing is commonly followed regardless of the type of MMC. However, a few factors must be considered when performing postprocessing for the LPBF-fabricated MMCs. As the requirements for the heating temperature and holding time for the composite materials differ even within the same heating method, a tailored strategy should be devised according to the specific matrix alloy in use. Moreover, the heat-treated microstructure of the MMCs undergo different mechanisms of evolution during the heat treatments. Understanding the microstructure recrystallization around reinforcements is essential for optimal postprocessing outcomes. Detailed information regarding the heat-treated microstructure of MMCs will be explored further in Section 3.2.

3. Microstructural Evolution of MMCs during LPBF and Heat Treatments

3.1. As-Built Microstructure of LPBF-Fabricated MMCs

3.1.1. Recrystallization Behavior of MMCs during LPBF Process

For certain particle-reinforced MMCs fabricated through LPBF, the grain refinement of the composites may be facilitated by the recrystallization behavior of partial grains. During the LPBF process, owing to the presence of a remelting process, which can be considered as an in situ annealing treatment, the recrystallization behavior may occur in some grains near the remelting areas, leading to an increase in the fraction of high-angle grain boundaries (HAGBs) [190]. Accordingly, it is meaningful to discuss the recrystallization behavior of matrix grains in this section.

Gao et al. [190] fabricated bimodal TiN nanoparticle-reinforced Al matrix composites based on the LPBF technique. They found that the recrystallization behavior of the matrix grains could be promoted by the existence of submicron TiN particles during the LPBF process (Figure 9a,c), and the growth of the recrystallized grains could be inhibited by TiN nanoparticles and HAGBs (Figure 9d). Therefore, the grains of the Al matrix can be efficiently refined when bimodal-sized reinforced particles are employed [191].

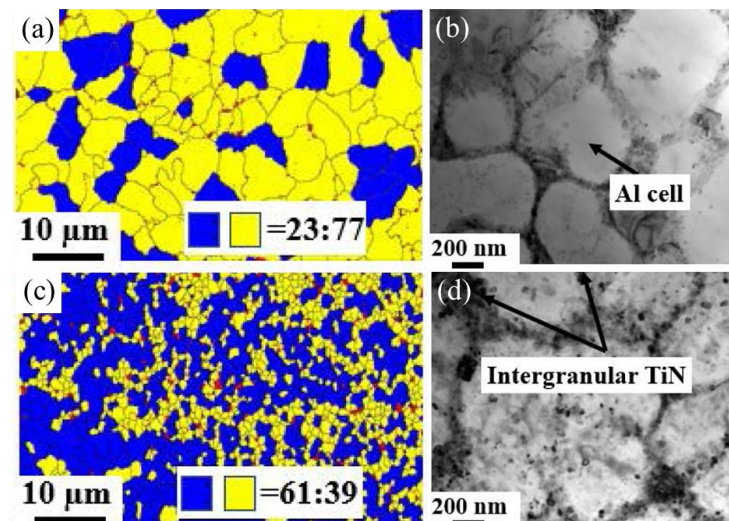


Figure 9. (a) Distribution of substructured (yellow) and recrystallized (blue) grains in AlSi10Mg alloys; (b) TEM bright-field (BF) image showing the Al matrix and Al + Si eutectic phase; (c) distribution of substructured and recrystallized grains in the TiN/AlSi10Mg nanocomposites; (d) TEM BF image showing the distribution of TiN nanoparticles in the Al matrix [190].

Similarly, the existence of large SiC nanoparticles was proven to induce the formation of fine recrystallized grains by providing effective nucleation sites for the matrix during the LPBF of nano-SiC/AlSi7Mg composites [192]. Yao et al. [193] studied the effect of micron-sized tungsten carbide (WC) particles on the microstructure and properties of LPBF-fabricated 18Ni300 steels. Some recrystallized grains were found to be produced by adding

15 wt.% WC particles, and they indicated that the residual stress and dislocation density of LPBF-fabricated composites could be reduced with the introduction of WC particles.

It can be concluded that the recrystallization phenomenon of matrix grains plays an important role in the microstructure and properties of LPBF-fabricated particle-reinforced MMCs, and the matrix containing larger particles ($>1 \mu\text{m}$) can possess a higher dislocation density and stored energy for recrystallization behavior. Therefore, it should be noted that sufficient submicron- or micron-sized particles can be designed to be formed in the matrix, because they can contribute to recrystallization behavior based on particle stimulated nucleation (PSN) [194]. In general, for the in situ heat treatment induced by the LPBF process, the existence of submicron and nanoparticles has the ability to block the movement of sub-grain boundaries as well as the rearrangement of dislocations, which can retard the recrystallization of matrix grains [177]. However, it was indicated that fine reinforced particles could also accelerate the recrystallization of matrix grains. Therefore, it is believed that the ratio (f_v/r) of volume fraction of particles (f_v) and particle radius (r) can be employed to evaluate the recrystallization behavior of grains for LPBF-fabricated particle-reinforced MMCs. If the ratio is below $0.2/\mu\text{m}$, the recrystallization phenomenon is prone to occur [195].

3.1.2. Diffusion and Interaction Behavior of Elements in High Temperature

Given that ultra-high temperatures can be induced in the molten pools during LPBF, the reinforced particles are more likely to undergo partial melting. Subsequently, some additional elements decomposed from particles can diffuse into the matrix, and some new precipitates may be formed. For example, NiTi-based composites were fabricated using the LPBF of powder mixture (Ti + Ni + TiC), and some Ni_4Ti_3 and Ni_3Ti precipitates were found to be formed in addition to the NiTi matrix and $\text{Ti}_6\text{C}_{3.75}$ particles, which was proved to can affect the pseudoelasticity recovery behavior of the matrix during nanoindentation [196]. Zhao et al. [197] employed SiC particles as reinforcements to strengthen AlSi10Mg alloys based on the LPBF technique, and Al_4SiC_4 precipitates were found to be generated in situ around some SiC particles. TiB_2 particles were introduced into LPBF-fabricated Inconel 718 alloys, and results showed that the phase precipitation behavior of alloys was changed from Laves phase to M_3B_2 boride particles, which effectively increased the hardness of alloys [198]. In addition, based on an in situ reaction, He et al. [199] obtained $\text{TiB} + \text{La}_2\text{O}_3/\text{Ti-6Al-4V}$ composites by the LPBF of a powder mixture of micro-sized LaB_6 particles and Ti-6Al-4V powder, and the formation of these precipitates was shown to enhance the tensile strength of alloys by impeding the movement of dislocations.

According to the aforementioned investigations, certain additional elements decomposed from particles are capable of reacting with the matrix elements to form precipitates, such as intermetallic compounds, oxides and carbides. In addition, some interfacial layers maybe be formed at the interface to affect the properties of materials, as discussed in a previous work [177].

Particularly, in terms of the elements decomposed from reinforced particles, it should be noted that the strength of MMCs can be affected by alterations in the chemical composition through solid solution strengthening. For example, researchers discovered that numerous TiC_xN_y nanoparticles were found to be produced within micron-sized TiC-reinforced duplex SS matrix composites fabricated through LPBF. Additionally, a reduction in the content of N elements within the matrix was observed. Hence, the strength improvement of composites can be weakened due to the loss of N elements in the matrix [185].

3.1.3. Elimination of Hot Cracks via the Addition of Reinforced Particles

During the LPBF of some alloys, coarse columnar grains often formed as a result of epitaxial grain growth, and the liquid film generated between these grains was prone to be torn apart by the thermal stress during the cooling of molten pools. In addition, the liquid film exhibited weak backfilling ability and fluidity. Therefore, the formation of hot cracks was reported in certain LPBF-fabricated alloys [200].

However, the addition of particles can achieve the elimination of hot cracks for some LPBF-fabricated alloys [201–203]. For instance, Liu et al. [204] employed TiC nanoparticles and TiH₂ powder as reinforcements to achieve grain refinement and crack inhibition of LPBF-fabricated Al alloys, and the formation of L1₂-Al₃Ti particles could provide heterogeneous nucleation sites for matrix grains. Subsequently, fine equiaxed α -Al grains were generated in composites compared to the LPBF-fabricated Al alloys with coarse columnar grains and cracks. This was believed to effectively mitigate the residual stress to inhibit the formation of hot cracks. Similarly, Han et al. [205] also indicated that the addition of TiC nanoparticles could achieve the intergranular microcrack elimination of LPBF-fabricated Hastelloy X nickel-based superalloys via grain refinement. Hot cracks formed in LPBF-fabricated Co₃₂Cr₃₆Ni₃₂ medium entropy alloys. However, it was proved that the introduction of micron-sized TiC particles could contribute to the formation of TiC nanoparticles and Cr₂₃C₆ precipitates at grain boundaries (GBs), which could inhibit the formation of hot cracks by reducing the GB energy and hot crack sensitivity of materials [206]. Particularly, the Zr element segregation at GBs was identified to induce the formation of hot cracks for LPBF-fabricated IN738LC nickel-based superalloys, while the employment of Y₂O₃ nanoparticles eliminated hot cracks. Some Y₄Al₂O₉ particles were produced for Y₂O₃-containing alloys, and Zr elements could substitute Y elements in these particles, reducing the Zr segregation at GBs to eliminate hot cracks [207].

According to the preceding discussion, it can be observed that the addition of reinforced particles plays a crucial role in the elimination of hot cracks for LPBF-fabricated alloys. Most importantly, eliminating cracks can effectively expand the process window for LPBF-fabricated metallic parts, serving as a promoter for the practical production of parts.

3.2. Heat-Treated Microstructure of LPBF-Fabricated MMCs

In heat treatment processes, achieving the anticipated phases can be challenging because of the rapid cooling rate and complex thermal history. To obtain the desired phases, specific post-heat treatment techniques must be implemented. For example, a significant proportion of ferrite phase (>99 vol%) is found in LPBF-fabricated duplex stainless-steel composites, necessitating a post quenching treatment [185].

A recrystallization behavior of MMCs is commonly observed in MMCs reinforced with micron-sized particles, particularly in areas where these particles are prevalent (Figure 10) [185]. This phenomenon is largely attributed to the initiation of particle-stimulated nucleation (PSN). In the LPBF-fabricated MMCs, the formation of fine equiaxed matrix grains has been often observed [208]. The growth of these grains typically occurs through the migration and coalescence of grain boundaries during the heat treatment. It is imperative to carefully regulate the heat treatment parameters to prevent a substantial decline in the mechanical properties of the MMCs. In addition, in instances where fine equiaxed grains are absent, there is potential for the grain orientation of MMCs to change, aligning with the grain growth.

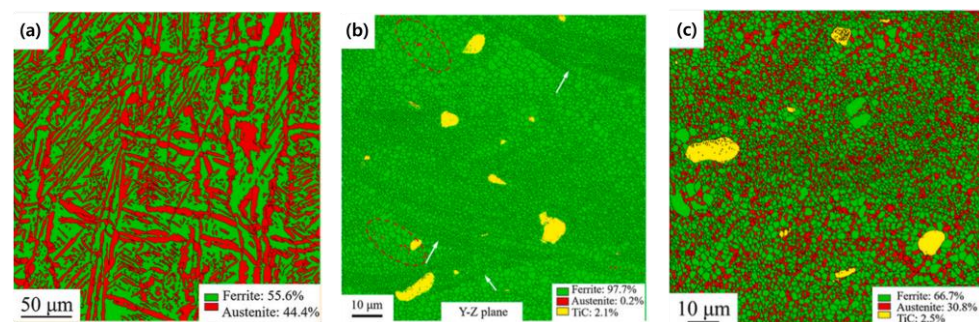


Figure 10. Phase maps: (a) heat-treated duplex stainless steel (DSS); (b) as-built DSS/TiC (3 wt.%); (c) heat-treated DSS/TiC (3 wt.%) [185]. Red dashed circles indicate the formation of austenite grains, and white arrows represent the fusion boundaries.

Specifically, for metals with an FCC crystal structure fabricated through LPBF, the $\langle 100 \rangle$ orientation is commonly favored as the primary direction for growth [209]. The majority of grains exhibiting this orientation tend to originate from the bottom of the molten pools [210]. Simultaneously, some grains may adopt a $\langle 110 \rangle$ orientation, spurred by alterations in the bottom curvature of the molten pools. It is worth noting that the post-heat treatment process can entirely alter the preferred growth direction of matrix grains to $\langle 110 \rangle$, transitioning from $\langle 110 \rangle$ to $\langle 100 \rangle$, since grains with a $\langle 100 \rangle$ texture are prioritized for growth. Consequently, this modification in grain orientation can have significant implications on the mechanical properties of heat-treated MMCs.

During the post-heat treatment, the diffusion and reaction of diverse elements can foster the development of particular precipitates. When carbide ceramic particles are utilized as reinforcements, carbon elements tend to dissolve into the MMC matrix, a consequence of the high temperatures and ultrafast cooling rates present during the LPBF process. This sets the stage for the generation of certain carbide precipitates, such as $M_{23}C_6$, fostered by the interactions and diffusion of carbon atoms with other atoms, like chromium, iron, and cobalt, during heat treatment.

4. Strengthening Mechanisms of LPBF-Fabricated MMCs

In terms of enhancing the strength of composites, it is vital to clarify some relevant strengthening mechanisms. Building upon several developed strengthening theories, the composites with high mechanical properties can be more effectively designed and fabricated utilizing the LPBF technique. Some classic strengthening mechanisms (fine grain, load transfer, dislocation, Orowan, and solid solution strengthening) will not be introduced in this section, and a relevant discussion can be found in our previous work [177]. With the advancement of particle-reinforced MMCs fabricated using LPBF, several novel strengthening theories have been proposed for the improvement of strength and ductility, such as special cellular substructure and heterogeneous structure.

First, it was found that the strength and ductility of TiC particle-reinforced 316L stainless steels (SSs) fabricated using LPBF could be simultaneously enhanced due to the formation of cellular sub-grains. This enhancement could be attributed to the fact that these unique substructures could increase the materials' plastic deformation ability and inhibit the propagation of microcracks [211,212]. Similarly, some intergranular ring-like structures surrounded by TiB_2 nanoparticles were proved to be able to simultaneously increase the strength and ductility of LPBF-fabricated $TiB_2/316L$ composites [213].

Second, during the LPBF of metals, the grain boundary (GB) segregation of elements is prone to be observed due to the ultra-high solidification process. Particularly, the contribution of elemental microsegregation to the material strength was proposed for the LPBF-fabricated $TiB_2/316L$ nanocomposites, which is called segregation engineering (σ_{se}) [208].

$$\sigma_{se} = \frac{\delta v_p}{\sqrt{d_{cell}}} \quad (2)$$

where δ represents a constant related to the segregated elements, d_{cell} is the boundary length of the cellular structure surrounded by the segregated elements, and v_p denotes the volume fraction of reinforced particles.

Third, the strength-ductility synergy can be achieved for LPBF-fabricated particle-reinforced MMCs by designing and fabricating a heterogeneous microstructure [214]. Li et al. [215] fabricated microlaminated CoCrFeNiMn high-entropy alloy (HEA) matrix composites with a bimodal grain size utilizing TiN nanoparticles and the LPBF technique (Figure 11a), and the strength–ductility trade-off of materials was successfully overcome. Three layers of pure HEA powder and powder mixture (5 wt.% TiN + 95 wt.% HEA) were printed alternately using multi-material selective-laser melting equipment (Figure 11a). Fine matrix grains were found to be formed between coarse matrix grains due to the numerous heterogeneous nucleation sites provided by TiN nanoparticles, as shown in Figure 10b. The results of the compressive split Hopkinson pressure bar (SHPB) tests

demonstrated that the microlaminated microstructure with bimodal grain size effectively improved the strength and ductility of HEAs at the same strain rate (Figure 11c).

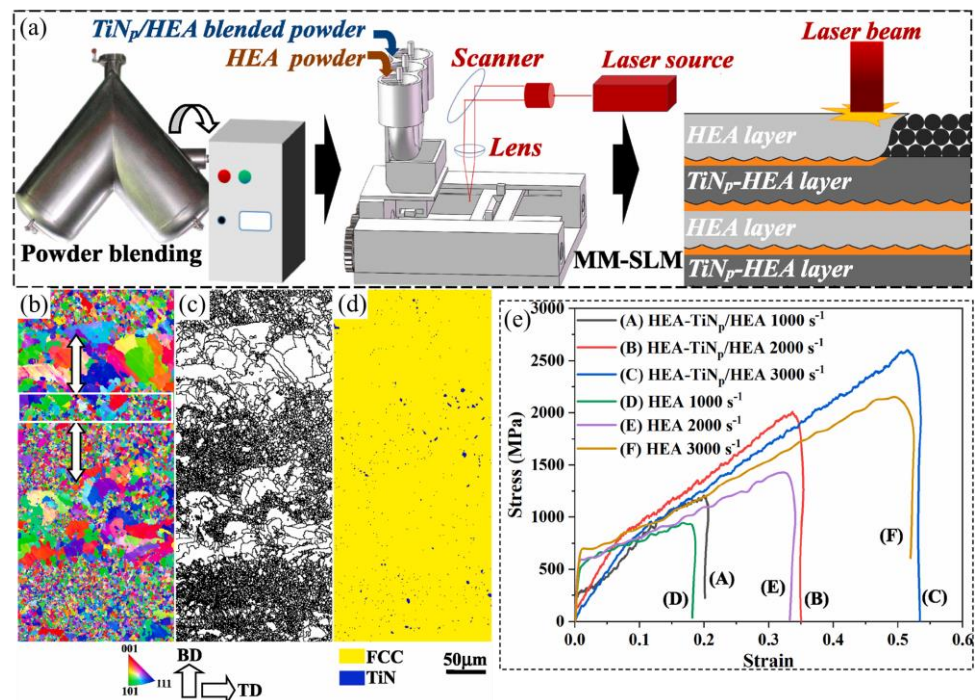


Figure 11. (a) Schematic of the fabrication procedure for microlaminated HEA-TiN/HEA via multi-material (MM) LPBF; (b) orientation map of the IPF of matrix grains for microlaminated HEA-TiN/HEA; (c) corresponding GB misorientation map; (d) corresponding phase map; (e) stress–strain curves of the SHPB impact test on LPBF-built HEA and MM-LPBF-built HEA-TiN/HEA with different nominal strain rates [215].

Therefore, it is meaningful and promising to introduce a heterogeneous microstructure, such as a heterogeneous lamella structure, gradient structure, and bimodal structure, into the LPBF-fabricated particle-reinforced MMCs. Because of the existence of back stress in the soft zone and forward stress in the hard zone, the hetero-deformation-induced (HDI) strengthening and HDI hardening can be formed by their interaction during deformation [214], as shown in Figure 12. The yield strength of materials can be enhanced by the HDI strengthening, and the HDI strain hardening is able to maintain or increase the material's ductility [216,217].

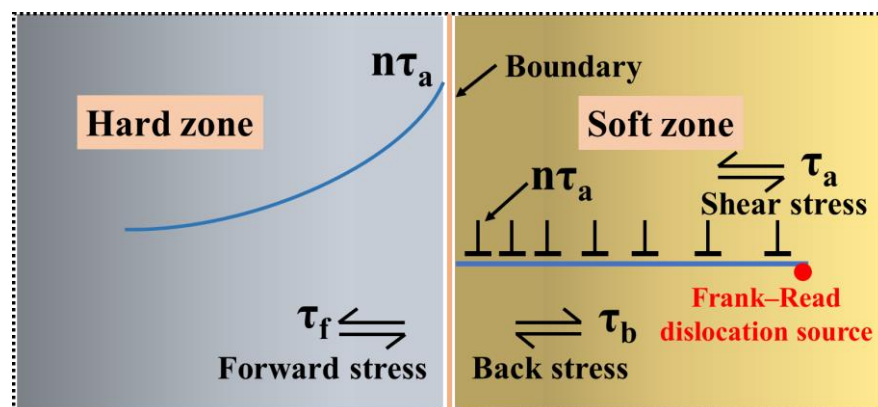


Figure 12. Schematic of the pile up of the geometrically necessary dislocations, and the formation of back stress in the soft zone and forward stress in the hard zone [218].

Finally, the yield strength of the materials can be affected by the variation in the texture, as shown by Equation (3) [219]:

$$\sigma = M\alpha bG\sqrt{\rho} \quad (3)$$

where M is the Taylor factor related to the material texture, α denotes a constant, b represents the Burgers vector, G is the shear modulus of matrix, and ρ denotes the dislocation density in the matrix. The texture of some LPBF-fabricated metals can be eliminated by the formation of equiaxed grains induced by reinforced particles, which is believed to be able to increase the strength of materials. For instance, a strong $\langle 100 \rangle$ texture always formed in some LPBF-fabricated metals with an FCC crystal structure [209]. Marattukalam et al. [220] indicated that there was a relatively low Taylor factor (2.3–2.6) for the LPBF-fabricated 316L SSs with a $\langle 100 \rangle$ texture, while a higher Taylor factor (~ 3.4) could be formed for the sample with a $\langle 110 \rangle$ texture. Therefore, in comparison with some LPBF-fabricated metals with a strong $\langle 100 \rangle$ texture, the yield strength of the LPBF-fabricated particle-reinforced MMCs without texture could be enhanced by an increase in the Taylor factor (Equation (3)).

5. A Summary of Strategies and Outlooks

5.1. Comprehensive Strategies Covering Material Selection to Processing

The fabrication of the particle-reinforced MMCs using LPBF requires the meticulous design of both the material and process to mitigate defects and enhance properties. Therefore, a strategy to prepare, design, and manufacture MMCs was discussed in this paper, as follows:

- (1) Material selection and preparation
 - ◆ The use of powder-type alloys and their moisture control are encouraged to ensure a good quality of the powder spreading and to prevent oxidation;
 - ◆ A material database of suitable combinations for matrices and reinforcements should be explored to meet the specific requirements of an application;
 - ◆ The compatibility of reinforcements within a matrix alloy needs to be investigated to prevent structural defects that result in premature failure caused by a poor bonding capability.
- (2) Process optimization
 - ◆ To obtain the designed phase in MMCs, the type of process atmosphere, such as N_2 and Ar atmospheres, is the major consideration in the LPBF process;
 - ◆ A fundamental understanding of the physical metallurgical phenomena associated with both the material and process is essential for mitigating defects, including pores, cracks, distortion, and delamination, during the LPBF process;
 - ◆ Various process parameters of LPBF should be systematically designed; recoating speed and layer thickness need to be set in the consideration of powder morphology and sizes; laser-related parameters must be designed on the basis of the characterization of melt pools and relative density.
- (3) Microstructure characterization
 - ◆ The mechanisms driving the microstructural evolution in LPBF-fabricated MMCs need to be understood, given their anisotropic and inhomogeneous properties;
 - ◆ The inclusion of nanoparticles, along with the existence of submicron- or micron-sized particles, can facilitate the recrystallization behavior of matrix grains, which refines the grains and reduces defects such as hot cracks;
 - ◆ Submicron- or micron-sized particles, formed in the matrix through PSN, can create new precipitates that improve hardness and strength by inhibiting dislocation movements;
 - ◆ Decomposed elements from the reinforced particles can alter the chemical composition of the matrix during the LPBF process, which significantly influences the material properties of MMCs.

(4) Postprocessing

- ◆ Postprocessing of the LPBF-fabricated MMCs generally follows the following sequence: a wire EDM, heat treatments, machining, and surface finishing;
- ◆ An unwanted as-built phase, induced by repetitive, high cooling rates, one might need to use heat treatments to obtain the desired phase of LPBF-fabricated MMCs through the recrystallization of the microstructure;
- ◆ Depending on the materials selected for applications, heat treatments should be carefully chosen to alleviate anisotropy, inhomogeneity, and residual stress, as well as to enhance properties;
- ◆ With the inclusion of particle reinforcements, phenomena such as grain refinement, elemental segregation, and texture management can occur during the heat treatment, thereby affecting the material properties.

5.2. Outlooks of LPBF-Fabricated MMCs

Some researchers have indicated that the use of nanoparticles could enhance the strength of alloys without compromising their ductility [221]. However, it is challenging to achieve the homogeneous distribution of the high content of nanoparticles in the matrix because of the van der Waals' forces between particles, which results in a limited increase in the strength of nano-MMCs. Therefore, considering the fabrication of hybrid reinforcements emerges as a promising and viable strategy to develop advanced MMCs. Specifically, multiscale (micron + submicron + nano) hybrid reinforcements should be pursued to realize synergistic effects based on the in situ synthesis phenomenon in the LPBF process.

The LPBF technique introduced in this paper emerges as an opportunity to realize high-performance composite materials for various industrial applications, including aerospace, automotive, nuclear power plants, and healthcare. However, significant challenges in LPBF still require extensive research regarding innovative materials and a comprehensive printing database to facilitate their manufacture. These challenges are attributed to several defects and the unwanted microstructure of MMCs produced by the repetitive, high cooling rates during the LPBF process.

Therefore, it is necessary to understand the physical metallurgical phenomena during the LPBF process and to systematically design the composite materials, LPBF processes, and postprocessing strategies. In situ monitoring or simulation techniques will promote a fundamental understanding of process-related phenomena. Incorporating artificial intelligence with the printing database may facilitate a deeper understanding of the complex interactions between various inputs and outputs associated with both the materials and the process. Based on these studies, a predictive model or standardized methodology for material processing is imperative for the wider industrial application of LPBF-fabricated MMCs.

Future research directions should emphasize collaborative work between academia and industry. Verifying the potential of LPBF-fabricated MMCs will bridge the gap between laboratory research and industrial applications, thereby fostering synergies between them.

Author Contributions: Conceptualization, M.-K.K. and Y.F.; writing—original draft preparation, M.-K.K. and Y.F.; writing—review and editing, M.-K.K., Y.F. and J.S.; literature survey, J.K., T.K., W.J. and Y.Z.; project administration, J.S.; funding acquisition, J.S. All authors have read and agreed to the published version of the manuscript.

Funding: This work was supported by a National Research Foundation of Korea (NRF) grant funded by the Korea government (MSIT) (No. 2022R1A2C3011968) and by the Air Force Office of Scientific Research, under grant number: FA2386-22-1-0104.

Data Availability Statement: No new data were created during this work.

Conflicts of Interest: The authors declare no conflict of interest.

References

1. Kim, M.-K.; Kim, T.; Kim, J.; Kim, D.; Fang, Y.; No, J.; Suhr, J. Selective Laser Melting of Metal Matrix Composites: A Review of Materials and Process Design. *Compos. Res.* **2021**, *34*, 212–225.
2. Hayat, M.D.; Singh, H.; He, Z.; Cao, P. Titanium metal matrix composites: An overview. *Compos. Part A Appl. Sci. Manuf.* **2019**, *121*, 418–438. [[CrossRef](#)]
3. Sharma, A.K.; Bhandari, R.; Aherwar, A.; Rimašauskienė, R.; Pinca-Bretotean, C. A study of advancement in application opportunities of aluminum metal matrix composites. *Mater. Today Proc.* **2020**, *26*, 2419–2424. [[CrossRef](#)]
4. Ramanathan, A.; Krishnan, P.K.; Muraliraja, R. A review on the production of metal matrix composites through stir casting—Furnace design, properties, challenges, and research opportunities. *J. Manuf. Process.* **2019**, *42*, 213–245. [[CrossRef](#)]
5. Gloria, A.; Montanari, R.; Richetta, M.; Varone, A. Alloys for aeronautic applications: State of the art and perspectives. *Metals* **2019**, *9*, 662. [[CrossRef](#)]
6. Gardner, L. The use of stainless steel in structures. *Prog. Struct. Eng. Mater.* **2005**, *7*, 45–55. [[CrossRef](#)]
7. Baddoo, N. Stainless steel in construction: A review of research, applications, challenges and opportunities. *J. Constr. Steel Res.* **2008**, *64*, 1199–1206. [[CrossRef](#)]
8. Gardner, L. Stability and design of stainless steel structures—Review and outlook. *Thin-Walled Struct.* **2019**, *141*, 208–216. [[CrossRef](#)]
9. Dursun, T.; Soutis, C. Recent developments in advanced aircraft aluminium alloys. *Mater. Des. (1980–2015)* **2014**, *56*, 862–871. [[CrossRef](#)]
10. Wahid, M.A.; Siddiquee, A.N.; Khan, Z.A. Aluminum alloys in marine construction: Characteristics, application, and problems from a fabrication viewpoint. *Mar. Syst. Ocean Technol.* **2020**, *15*, 70–80. [[CrossRef](#)]
11. Ezugwu, E.; Wang, Z.; Machado, A. The machinability of nickel-based alloys: A review. *J. Mater. Process. Technol.* **1999**, *86*, 1–16. [[CrossRef](#)]
12. Balitskii, O.; Kvasnytska, Y.H.; Ivaskevych, L.; Mialnitsa, H.; Kvasnytska, K. Fatigue fracture of the blades of gas-turbine engines made of a new refractory nickel alloy. *Mater. Sci.* **2022**, *57*, 475–483. [[CrossRef](#)]
13. Zhang, L.C.; Chen, L.Y. A review on biomedical titanium alloys: Recent progress and prospect. *Adv. Eng. Mater.* **2019**, *21*, 1801215. [[CrossRef](#)]
14. Bai, H.; Zhong, L.; Kang, L.; Liu, J.; Zhuang, W.; Lv, Z.; Xu, Y. A review on wear-resistant coating with high hardness and high toughness on the surface of titanium alloy. *J. Alloys Compd.* **2021**, *882*, 160645. [[CrossRef](#)]
15. Nicholson, J.W. Titanium alloys for dental implants: A review. *Prosthesis* **2020**, *2*, 100–116. [[CrossRef](#)]
16. Williams, J.C.; Boyer, R.R. Opportunities and issues in the application of titanium alloys for aerospace components. *Metals* **2020**, *10*, 705. [[CrossRef](#)]
17. Casati, R.; Vedani, M. Metal matrix composites reinforced by nano-particles—A review. *Metals* **2014**, *4*, 65–83. [[CrossRef](#)]
18. Bhoi, N.K.; Singh, H.; Pratap, S. Developments in the aluminum metal matrix composites reinforced by micro/nano particles—A review. *J. Compos. Mater.* **2020**, *54*, 813–833. [[CrossRef](#)]
19. Merino, C.A.I.; Sillas, J.L.; Meza, J.; Ramirez, J.H. Metal matrix composites reinforced with carbon nanotubes by an alternative technique. *J. Alloys Compd.* **2017**, *707*, 257–263. [[CrossRef](#)]
20. Alam, S.N.; Kumar, L. Mechanical properties of aluminium based metal matrix composites reinforced with graphite nanoplatelets. *Mater. Sci. Eng. A* **2016**, *667*, 16–32. [[CrossRef](#)]
21. Cooper, D.E.; Blundell, N.; Maggs, S.; Gibbons, G.J. Additive layer manufacture of Inconel 625 metal matrix composites, reinforcement material evaluation. *J. Mater. Process. Technol.* **2013**, *213*, 2191–2200. [[CrossRef](#)]
22. Kim, M.-K.; Kim, H.-I.; Nam, J.-D.; Suhr, J. Polyamide-nylon 6 particulate polycarbonate composites with outstanding energy-absorbing properties. *Polymer* **2022**, *254*, 125082. [[CrossRef](#)]
23. Gu, D.; Shi, X.; Poprawe, R.; Bourell, D.L.; Setchi, R.; Zhu, J. Material-structure-performance integrated laser-metal additive manufacturing. *Science* **2021**, *372*, eabg1487. [[CrossRef](#)] [[PubMed](#)]
24. Zhao, D.; Yu, K.; Sun, T.; Jing, X.; Wan, Y.; Chen, K.; Gao, H.; Wang, Y.; Chen, L.; Guo, X. Material-Structure-Function Integrated Additive Manufacturing of Degradable Metallic Bone Implants for Load-Bearing Applications. *Adv. Funct. Mater.* **2023**, *33*, 2213128. [[CrossRef](#)]
25. Wang, Y.M.; Voisin, T.; McKeown, J.T.; Ye, J.; Calta, N.P.; Li, Z.; Zeng, Z.; Zhang, Y.; Chen, W.; Roehling, T.T. Additively manufactured hierarchical stainless steels with high strength and ductility. *Nat. Mater.* **2018**, *17*, 63–71. [[CrossRef](#)] [[PubMed](#)]
26. Hirt, L.; Reiser, A.; Spolenak, R.; Zambelli, T. Additive manufacturing of metal structures at the micrometer scale. *Adv. Mater.* **2017**, *29*, 1604211. [[CrossRef](#)]
27. Barriobero-Vila, P.; Vallejos, J.M.; Gussone, J.; Haubrich, J.; Kelm, K.; Stark, A.; Schell, N.; Requena, G. Interface-Mediated Twinning-Induced Plasticity in a Fine Hexagonal Microstructure Generated by Additive Manufacturing. *Adv. Mater.* **2021**, *33*, 2105096. [[CrossRef](#)]
28. Ren, J.; Zhang, Y.; Zhao, D.; Chen, Y.; Guan, S.; Liu, Y.; Liu, L.; Peng, S.; Kong, F.; Poplawsky, J.D. Strong yet ductile nanolamellar high-entropy alloys by additive manufacturing. *Nature* **2022**, *608*, 62–68. [[CrossRef](#)]
29. Kwon, J.; Karthik, G.; Estrin, Y.; Kim, H.S. Constitutive modeling of cellular-structured metals produced by additive manufacturing. *Acta Mater.* **2022**, *241*, 118421. [[CrossRef](#)]

30. Yao, N.; Lu, T.; Feng, K.; Sun, B.; Wang, R.-Z.; Wang, J.; Xie, Y.; Zhao, P.; Han, B.; Zhang, X.-C. Ultrastrong and ductile additively manufactured precipitation-hardening medium-entropy alloy at ambient and cryogenic temperatures. *Acta Mater.* **2022**, *236*, 118142. [[CrossRef](#)]
31. Lin, T.-C.; Cao, C.; Sokoluk, M.; Jiang, L.; Wang, X.; Schoenung, J.M.; Lavernia, E.J.; Li, X. Aluminum with dispersed nanoparticles by laser additive manufacturing. *Nat. Commun.* **2019**, *10*, 4124. [[CrossRef](#)] [[PubMed](#)]
32. Hou, H.; Simsek, E.; Ma, T.; Johnson, N.S.; Qian, S.; Cissé, C.; Stasak, D.; Al Hasan, N.; Zhou, L.; Hwang, Y. Fatigue-resistant high-performance elastocaloric materials made by additive manufacturing. *Science* **2019**, *366*, 1116–1121. [[CrossRef](#)] [[PubMed](#)]
33. Liu, Y.; Ren, J.; Guan, S.; Li, C.; Zhang, Y.; Muskeri, S.; Liu, Z.; Yu, D.; Chen, Y.; An, K. Microstructure and mechanical behavior of additively manufactured CoCrFeMnNi high-entropy alloys: Laser directed energy deposition versus powder bed fusion. *Acta Mater.* **2023**, *250*, 118884. [[CrossRef](#)]
34. Bae, J.; Kim, M.-k.; Oh, E.; Yang, K.-T.; Suhr, J. Experimental and numerical investigation of 17–4PH stainless steel fabricated by laser powder bed fusion and hot isostatic pressing. *Mater. Res. Express* **2021**, *8*, 106512. [[CrossRef](#)]
35. Todd, I. No more tears for metal 3D printing. *Nature* **2017**, *549*, 342–343. [[CrossRef](#)]
36. Bonnín Roca, J.; Vaishnav, P.; Fuchs, E.R.; Morgan, M.G. Policy needed for additive manufacturing. *Nat. Mater.* **2016**, *15*, 815–818. [[CrossRef](#)]
37. DebRoy, T.; Mukherjee, T.; Milewski, J.; Elmer, J.; Ribic, B.; Blecher, J.; Zhang, W. Scientific, technological and economic issues in metal printing and their solutions. *Nat. Mater.* **2019**, *18*, 1026–1032. [[CrossRef](#)]
38. Khairallah, S.A.; Anderson, A.T.; Rubenchik, A.; King, W.E. Laser powder-bed fusion additive manufacturing: Physics of complex melt flow and formation mechanisms of pores, spatter, and denudation zones. *Acta Mater.* **2016**, *108*, 36–45. [[CrossRef](#)]
39. Zhao, Y.; Ma, Z.; Yu, L.; Liu, Y. New alloy design approach to inhibiting hot cracking in laser additive manufactured nickel-based superalloys. *Acta Mater.* **2023**, *247*, 118736. [[CrossRef](#)]
40. Qiu, C.; Panwisawas, C.; Ward, M.; Basoalto, H.C.; Brooks, J.W.; Attallah, M.M. On the role of melt flow into the surface structure and porosity development during selective laser melting. *Acta Mater.* **2015**, *96*, 72–79. [[CrossRef](#)]
41. Chakraborty, A.; Muhammad, W.; Masse, J.-P.; Tangestani, R.; Ghasri-Khouzani, M.; Wessman, A.; Martin, É. Role of alloy composition on micro-cracking mechanisms in additively manufactured Ni-based superalloys. *Acta Mater.* **2023**, *255*, 119089. [[CrossRef](#)]
42. Khairallah, S.A.; Martin, A.A.; Lee, J.R.; Guss, G.; Calt, N.P.; Hammons, J.A.; Nielsen, M.H.; Chaput, K.; Schwalbach, E.; Shah, M.N. Controlling interdependent meso-nanosecond dynamics and defect generation in metal 3D printing. *Science* **2020**, *368*, 660–665. [[CrossRef](#)] [[PubMed](#)]
43. Matthews, M.J.; Guss, G.; Khairallah, S.A.; Rubenchik, A.M.; Depond, P.J.; King, W.E. Denudation of metal powder layers in laser powder-bed fusion processes. In *Additive Manufacturing Handbook*; CRC Press: Boca Raton, FL, USA, 2017; pp. 677–692.
44. Chia, H.Y.; Wang, L.; Yan, W. Influence of oxygen content on melt pool dynamics in metal additive manufacturing: High-fidelity modeling with experimental validation. *Acta Mater.* **2023**, *249*, 118824. [[CrossRef](#)]
45. Chen, H.; Cheng, T.; Li, Z.; Wei, Q.; Yan, W. Is high-speed powder spreading really unfavourable for the part quality of laser powder bed fusion additive manufacturing? *Acta Mater.* **2022**, *231*, 117901. [[CrossRef](#)]
46. Panwisawas, C.; Perumal, B.; Ward, R.M.; Turner, N.; Turner, R.P.; Brooks, J.W.; Basoalto, H.C. Keyhole formation and thermal fluid flow-induced porosity during laser fusion welding in titanium alloys: Experimental and modelling. *Acta Mater.* **2017**, *126*, 251–263. [[CrossRef](#)]
47. Johnson, L.; Mahmoudi, M.; Zhang, B.; Seede, R.; Huang, X.; Maier, J.T.; Maier, H.J.; Karaman, I.; Elwany, A.; Arróyave, R. Assessing printability maps in additive manufacturing of metal alloys. *Acta Mater.* **2019**, *176*, 199–210. [[CrossRef](#)]
48. Shinjo, J.; Panwisawas, C. Digital materials design by thermal-fluid science for multi-metal additive manufacturing. *Acta Mater.* **2021**, *210*, 116825. [[CrossRef](#)]
49. Yan, W.; Ge, W.; Qian, Y.; Lin, S.; Zhou, B.; Liu, W.K.; Lin, F.; Wagner, G.J. Multi-physics modeling of single/multiple-track defect mechanisms in electron beam selective melting. *Acta Mater.* **2017**, *134*, 324–333. [[CrossRef](#)]
50. Lu, L.-X.; Sridhar, N.; Zhang, Y.-W. Phase field simulation of powder bed-based additive manufacturing. *Acta Mater.* **2018**, *144*, 801–809. [[CrossRef](#)]
51. Martin, J.H.; Barnes, J.E.; Rogers, K.A.; Hundley, J.; LaPlant, D.L.; Ghanbari, S.; Tsai, J.-T.; Bahr, D.F. Additive manufacturing of a high-performance aluminum alloy from cold mechanically derived non-spherical powder. *Commun. Mater.* **2023**, *4*, 39. [[CrossRef](#)]
52. Chen, H.; Wei, Q.; Zhang, Y.; Chen, F.; Shi, Y.; Yan, W. Powder-spreading mechanisms in powder-bed-based additive manufacturing: Experiments and computational modeling. *Acta Mater.* **2019**, *179*, 158–171. [[CrossRef](#)]
53. Zhao, C.; Parab, N.D.; Li, X.; Fezzaa, K.; Tan, W.; Rollett, A.D.; Sun, T. Critical instability at moving keyhole tip generates porosity in laser melting. *Science* **2020**, *370*, 1080–1086. [[CrossRef](#)] [[PubMed](#)]
54. Cunningham, R.; Zhao, C.; Parab, N.; Kantzos, C.; Pauza, J.; Fezzaa, K.; Sun, T.; Rollett, A.D. Keyhole threshold and morphology in laser melting revealed by ultrahigh-speed x-ray imaging. *Science* **2019**, *363*, 849–852. [[CrossRef](#)] [[PubMed](#)]
55. Ren, Z.; Gao, L.; Clark, S.J.; Fezzaa, K.; Shevchenko, P.; Choi, A.; Everhart, W.; Rollett, A.D.; Chen, L.; Sun, T. Machine learning-aided real-time detection of keyhole pore generation in laser powder bed fusion. *Science* **2023**, *379*, 89–94. [[CrossRef](#)] [[PubMed](#)]
56. Chen, H.; Yan, W. Spattering and denudation in laser powder bed fusion process: Multiphase flow modelling. *Acta Mater.* **2020**, *196*, 154–167. [[CrossRef](#)]

57. Sun, Z.; Ma, Y.; Ponge, D.; Zaefferer, S.; Jäggle, E.A.; Gault, B.; Rollett, A.D.; Raabe, D. Thermodynamics-guided alloy and process design for additive manufacturing. *Nat. Commun.* **2022**, *13*, 4361. [[CrossRef](#)]
58. Guo, Q.; Zhao, C.; Escano, L.I.; Young, Z.; Xiong, L.; Fezzaa, K.; Everhart, W.; Brown, B.; Sun, T.; Chen, L. Transient dynamics of powder spattering in laser powder bed fusion additive manufacturing process revealed by in-situ high-speed high-energy x-ray imaging. *Acta Mater.* **2018**, *151*, 169–180. [[CrossRef](#)]
59. Van Cauwenbergh, P.; Samaee, V.; Thijs, L.; Nejezchlebová, J.; Sedlak, P.; Iveković, A.; Schryvers, D.; Van Hooreweder, B.; Vanmeensel, K. Unravelling the multi-scale structure–property relationship of laser powder bed fusion processed and heat-treated AlSi10Mg. *Sci. Rep.* **2021**, *11*, 6423. [[CrossRef](#)]
60. Newell, D.J.; O’Hara, R.P.; Cobb, G.R.; Palazotto, A.N.; Kirka, M.M.; Burggraf, L.W.; Hess, J.A. Mitigation of scan strategy effects and material anisotropy through supersolvus annealing in LPBF IN718. *Mater. Sci. Eng. A* **2019**, *764*, 138230. [[CrossRef](#)]
61. Qu, S.; Ding, J.; Fu, J.; Fu, M.; Song, X. Anisotropic material properties of pure copper with fine-grained microstructure fabricated by laser powder bed fusion process. *Addit. Manuf.* **2022**, *59*, 103082. [[CrossRef](#)]
62. Gokcekaya, O.; Ishimoto, T.; Hibino, S.; Yasutomi, J.; Narushima, T.; Nakano, T. Unique crystallographic texture formation in Inconel 718 by laser powder bed fusion and its effect on mechanical anisotropy. *Acta Mater.* **2021**, *212*, 116876. [[CrossRef](#)]
63. Dehgahi, S.; Pirgazi, H.; Sanjari, M.; Seraj, P.; Odeshi, A.; Kestens, L.; Mohammadi, M. Effect of building direction on high strain-rate compressive behavior of heat-treated LPBF-maraging steels using Split Hopkinson pressure bar apparatus. *Mater. Sci. Eng. A* **2022**, *835*, 142653. [[CrossRef](#)]
64. Pérez-Ruiz, J.D.; de Lacalle, L.N.L.; Urbikain, G.; Pereira, O.; Martínez, S.; Bris, J. On the relationship between cutting forces and anisotropy features in the milling of LPBF Inconel 718 for near net shape parts. *Int. J. Mach. Tools Manuf.* **2021**, *170*, 103801. [[CrossRef](#)]
65. Aota, L.S.; Bajaj, P.; Zilnyk, K.D.; Ponge, D.; Sandim, H.R.Z. The origin of abnormal grain growth upon thermomechanical processing of laser powder-bed fusion alloys. *Materialia* **2021**, *20*, 101243. [[CrossRef](#)]
66. Qin, H.; Fallah, V.; Dong, Q.; Brochu, M.; Daymond, M.R.; Gallerneault, M. Solidification pattern, microstructure and texture development in Laser Powder Bed Fusion (LPBF) of Al10SiMg alloy. *Mater. Charact.* **2018**, *145*, 29–38. [[CrossRef](#)]
67. Sun, S.; Teng, Q.; Xie, Y.; Liu, T.; Ma, R.; Bai, J.; Cai, C.; Wei, Q. Two-step heat treatment for laser powder bed fusion of a nickel-based superalloy with simultaneously enhanced tensile strength and ductility. *Addit. Manuf.* **2021**, *46*, 102168. [[CrossRef](#)]
68. Marchese, G.; Parizia, S.; Rashidi, M.; Saboori, A.; Manfredi, D.; Ugues, D.; Lombardi, M.; Hryha, E.; Biamino, S. The role of texturing and microstructure evolution on the tensile behavior of heat-treated Inconel 625 produced via laser powder bed fusion. *Mater. Sci. Eng. A* **2020**, *769*, 138500. [[CrossRef](#)]
69. Serrano-Munoz, I.; Fritsch, T.; Mishurova, T.; Trofimov, A.; Apel, D.; Ulbricht, A.; Kromm, A.; Hesse, R.; Evans, A.; Bruno, G. On the interplay of microstructure and residual stress in LPBF IN718. *J. Mater. Sci.* **2021**, *56*, 5845–5867. [[CrossRef](#)]
70. Cao, S.; Zou, Y.; Lim, C.V.S.; Wu, X. Review of laser powder bed fusion (LPBF) fabricated Ti-6Al-4V: Process, post-process treatment, microstructure, and property. *Light Adv. Manuf.* **2021**, *2*, 313–332. [[CrossRef](#)]
71. Krakhmalev, P.; Fredriksson, G.; Svensson, K.; Yadroitsev, I.; Yadroitsava, I.; Thuvander, M.; Peng, R. Microstructure, solidification texture, and thermal stability of 316 L stainless steel manufactured by laser powder bed fusion. *Metals* **2018**, *8*, 643. [[CrossRef](#)]
72. Dikova, T. *Properties of Co-Cr Dental Alloys Fabricated using Additive Technologies*; IntechOpen: London, UK, 2018; Volume 1.
73. Sidambe, A.; Tian, Y.; Prangnell, P.; Fox, P. Effect of processing parameters on the densification, microstructure and crystallographic texture during the laser powder bed fusion of pure tungsten. *Int. J. Refract. Met. Hard Mater.* **2019**, *78*, 254–263. [[CrossRef](#)]
74. Colosimo, B.M.; Grasso, M. In-situ monitoring in L-PBF: Opportunities and challenges. *Procedia CIRP* **2020**, *94*, 388–391. [[CrossRef](#)]
75. Li, Z.; Mizutani, M. Influence of layer thickness and substrate bed on the void fraction of powder layers for laser powder bed fusion. *Powder Technol.* **2023**, *418*, 118293. [[CrossRef](#)]
76. Balbaa, M.; Ghasemi, A.; Fereiduni, E.; Elbestawi, M.; Jadhav, S.; Kruth, J.-P. Role of powder particle size on laser powder bed fusion processability of AlSi10mg alloy. *Addit. Manuf.* **2021**, *37*, 101630. [[CrossRef](#)]
77. Mussatto, A.; Groarke, R.; O’Neill, A.; Obeidi, M.A.; Delaure, Y.; Brabazon, D. Influences of powder morphology and spreading parameters on the powder bed topography uniformity in powder bed fusion metal additive manufacturing. *Addit. Manuf.* **2021**, *38*, 101807. [[CrossRef](#)]
78. Badrossamay, M.; Rezaei, A.; Foroozmehr, E.; Maleki, A.; Foroozmehr, A. Effects of increasing powder layer thickness on the microstructure, mechanical properties, and failure mechanism of IN718 superalloy fabricated by laser powder bed fusion. *Int. J. Adv. Manuf. Technol.* **2021**, *118*, 1703–1717. [[CrossRef](#)]
79. Mahmoodkhani, Y.; Ali, U.; Imani Shahabad, S.; Rani Kasinathan, A.; Esmailizadeh, R.; Keshavarzkermani, A.; Marzbanrad, E.; Toyserkani, E. On the measurement of effective powder layer thickness in laser powder-bed fusion additive manufacturing of metals. *Prog. Addit. Manuf.* **2019**, *4*, 109–116. [[CrossRef](#)]
80. Narra, S.P.; Wu, Z.; Patel, R.; Capone, J.; Paliwal, M.; Beuth, J.; Rollett, A. Use of non-spherical hydride-dehydride (HDH) powder in powder bed fusion additive manufacturing. *Addit. Manuf.* **2020**, *34*, 101188. [[CrossRef](#)]
81. Asherloo, M.; Hwang, J.; Leroux, R.; Wu, Z.; Fezzaa, K.; Paliwal, M.; Rollett, A.D.; Mostafaei, A. Understanding process-microstructure-property relationships in laser powder bed fusion of non-spherical Ti-6Al-4V powder. *Mater. Charact.* **2023**, *198*, 112757. [[CrossRef](#)]

82. Asherloo, M.; Wu, Z.; Delpazir, M.H.; Ghebreiesus, E.; Fryzlewicz, S.; Jiang, R.; Gould, B.; Heim, M.; Nelson, D.; Marucci, M. Laser-beam powder bed fusion of cost-effective non-spherical hydride-dehydride Ti-6Al-4V alloy. *Addit. Manuf.* **2022**, *56*, 102875. [[CrossRef](#)]
83. Wang, X.; Zhang, Y.; Du, D.; Dong, A.; Sun, B.; Chen, Z.; Zheng, X.; Wang, X.; Liu, Y.; Zhou, J. Evolutionary behavior of Haynes 230 powder during laser powder bed fusion cycle and its effect on the mechanical performance of manufactured parts. *Mater. Today Commun.* **2023**, *34*, 105384. [[CrossRef](#)]
84. Snow, Z.; Martukanitz, R.; Joshi, S. On the development of powder spreadability metrics and feedstock requirements for powder bed fusion additive manufacturing. *Addit. Manuf.* **2019**, *28*, 78–86. [[CrossRef](#)]
85. Gao, X.; Faria, G.A.; Zhang, W.; Wheeler, K.R. Numerical analysis of non-spherical particle effect on molten pool dynamics in laser-powder bed fusion additive manufacturing. *Comput. Mater. Sci.* **2020**, *179*, 109648. [[CrossRef](#)]
86. Guzmán, J.; de Moura Nobre, R.; Rodrigues Júnior, D.L.; de Moraes, W.A.; Nunes, E.R.; Bayerlein, D.L.; Falcao, R.; Sallica-Leva, E.; Oliveira, H.R.; Chastinet, V.L. Comparing spherical and irregularly shaped powders in laser powder bed fusion of Nb47Ti alloy. *J. Mater. Eng. Perform.* **2021**, *30*, 6557–6567. [[CrossRef](#)]
87. Haferkamp, L.; Haudenschild, L.; Spierings, A.; Wegener, K.; Riener, K.; Ziegelmeier, S.; Leichtfried, G.J. The influence of particle shape, powder flowability, and powder layer density on part density in laser powder bed fusion. *Metals* **2021**, *11*, 418. [[CrossRef](#)]
88. Vasquez, E.; Giroux, P.-F.; Lomello, F.; Nussbaum, M.; Maskrot, H.; Schuster, F.; Castany, P. Effect of powder characteristics on production of oxide dispersion strengthened Fe14Cr steel by laser powder bed fusion. *Powder Technol.* **2020**, *360*, 998–1005. [[CrossRef](#)]
89. Zhou, W.; Sun, X.; Kikuchi, K.; Nomura, N.; Yoshimi, K.; Kawasaki, A. In situ synthesized TiC/Mo-based composites via laser powder bed fusion. *Mater. Des.* **2018**, *146*, 116–124. [[CrossRef](#)]
90. Yin, H.; Yang, J.; Zhang, Y.; Crilly, L.; Jackson, R.L.; Lou, X. Carbon nanotube (CNT) reinforced 316L stainless steel composites made by laser powder bed fusion: Microstructure and wear response. *Wear* **2022**, *496*, 204281. [[CrossRef](#)]
91. Zhou, W.; Kamata, K.; Dong, M.; Nomura, N. Laser powder bed fusion additive manufacturing, microstructure evolution, and mechanical performance of carbon nanotube-decorated titanium alloy powders. *Powder Technol.* **2021**, *382*, 274–283. [[CrossRef](#)]
92. Lee, E.R.; Shin, S.E.; Takata, N.; Kobashi, M.; Kato, M. Manufacturing aluminum/multiwalled carbon nanotube composites via laser powder bed fusion. *Materials* **2020**, *13*, 3927. [[CrossRef](#)]
93. Yoo, S.; Shin, S.-E.; Takata, N.; Kobashi, M. Aluminum matrix composites reinforced with multi-walled carbon nanotubes and C60 manufactured by laser powder bed fusion. *J. Mater. Sci.* **2022**, *57*, 17984–17999. [[CrossRef](#)]
94. Zhang, S.; Wei, P.; Chen, Z.; Li, B.; Huang, K.; Zou, Y.; Lu, B. Graphene/ZrO₂/aluminum alloy composite with enhanced strength and ductility fabricated by laser powder bed fusion. *J. Alloys Compd.* **2022**, *910*, 164941. [[CrossRef](#)]
95. Zhang, Q.; Sun, W.; Xu, S.; Zhang, X.; Wang, J.; Si, C. Nano-TiB whiskers reinforced Ti-6Al-4 V matrix composite fabricated by direct laser deposition: Microstructure and mechanical properties. *J. Alloys Compd.* **2022**, *922*, 166171. [[CrossRef](#)]
96. Sun, X.; Chen, M.; Liu, D. Fabrication and characterization of few-layer graphene oxide reinforced magnesium matrix composites. *Mater. Sci. Eng. A* **2021**, *803*, 140722. [[CrossRef](#)]
97. Mandal, A.; Tiwari, J.K.; AlMangour, B.; Das, A.; Sathish, N.; Sharma, R.; Rajput, P.; Srivastava, A. Microstructural and thermal expansion behaviour of graphene reinforced 316L stainless steel matrix composite prepared via powder bed fusion additive manufacturing. *Results Mater.* **2021**, *11*, 100200. [[CrossRef](#)]
98. Xue, G.; Ke, L.; Liao, H.; Chen, C.; Zhu, H. Effect of SiC particle size on densification behavior and mechanical properties of SiCp/AlSi10Mg composites fabricated by laser powder bed fusion. *J. Alloys Compd.* **2020**, *845*, 156260. [[CrossRef](#)]
99. Niu, X.; Shen, H.; Fu, J.; Feng, J. Effective control of microstructure evolution in AZ91D magnesium alloy by SiC nanoparticles in laser powder-bed fusion. *Mater. Des.* **2021**, *206*, 109787. [[CrossRef](#)]
100. Stylianou, R.; Evangelou, A.; Loizou, A.; Kim, D.; Wharton, J.; Koutsokeras, L.; Constantinides, G.; Delimitis, A.; Kyratsi, T. Laser powder bed fusion of 316 L stainless steel with 2 wt.% nanosized SiO₂ additives: Powder processing and consolidation. *Powder Technol.* **2023**, *427*, 118714. [[CrossRef](#)]
101. Akilan, A.A.; Gökçe, A.; Nath, S.D.; Balla, V.K.; Kate, K.H.; Atre, S.V. Laser powder bed fusion of in-situ composites using dry-mixed Ti6Al4V and Si₃N₄ powder. *J. Manuf. Process.* **2020**, *59*, 43–50. [[CrossRef](#)]
102. Du, Z.; Chen, H.-C.; Tan, M.J.; Bi, G.; Chua, C.K. Effect of n Al₂O₃ on the part density and microstructure during the laser-based powder bed fusion of AlSi₁₀Mg composite. *Rapid Prototyp. J.* **2020**, *26*, 727–735. [[CrossRef](#)]
103. Reinhart, A.; Ansell, T.; Smith, W.; Nieto, A. Oxide Reinforced Ti64 Composites Processed by Selective Laser Melting. *J. Mater. Eng. Perform.* **2021**, *30*, 6949–6960. [[CrossRef](#)]
104. Dai, D.; Gu, D. Influence of thermodynamics within molten pool on migration and distribution state of reinforcement during selective laser melting of AlN/AlSi10Mg composites. *Int. J. Mach. Tools Manuf.* **2016**, *100*, 14–24. [[CrossRef](#)]
105. Mandal, V.; Tripathi, P.; Kumar, A.; Singh, S.S.; Ramkumar, J. A study on selective laser melting (SLM) of TiC and B4C reinforced IN718 metal matrix composites (MMCs). *J. Alloys Compd.* **2022**, *901*, 163527. [[CrossRef](#)]
106. Fereiduni, E.; Ghasemi, A.; Elbestawi, M. TiB reinforced Ti-6Al-4V matrix composites with improved short-term creep performance fabricated by laser powder bed fusion. *J. Manuf. Process.* **2021**, *70*, 593–607. [[CrossRef](#)]
107. Zhang, Z.; Han, Q.; Yang, S.; Yin, Y.; Gao, J.; Setchi, R. Laser powder bed fusion of advanced submicrometer TiB₂ reinforced high-performance Ni-based composite. *Mater. Sci. Eng. A* **2021**, *817*, 141416. [[CrossRef](#)]

108. Ghodsi, M.; Khademzadeh, S.; Marzbanrad, E.; Razmpoosh, M.; De Marchi, N.; Toyserkani, E. Development of Ytria-stabilized zirconia reinforced Inconel 625 metal matrix composite by laser powder bed fusion. *Mater. Sci. Eng. A* **2021**, *827*, 142037. [[CrossRef](#)]
109. Mair, P.; Kaserer, L.; Braun, J.; Weinberger, N.; Letofsky-Papst, I.; Leichtfried, G. Microstructure and mechanical properties of a TiB₂-modified Al–Cu alloy processed by laser powder-bed fusion. *Mater. Sci. Eng. A* **2021**, *799*, 140209. [[CrossRef](#)]
110. Shi, Q.; Mertens, R.; Dadbakhsh, S.; Li, G.; Yang, S. In-situ formation of particle reinforced Aluminium matrix composites by laser powder bed fusion of Fe₂O₃/AlSi12 powder mixture using laser melting/remelting strategy. *J. Mater. Process. Technol.* **2022**, *299*, 117357. [[CrossRef](#)]
111. Ng, C.K.; Bai, K.; Wu, D.; Lau, K.B.; Lee, J.J.; Cheong, A.K.H.; Wei, F.; Cheng, B.; Wang, P.; Tan, D.C.C. Additive manufacturing of high-strength and ductile high entropy alloy CoCrFeNiW_{0.2} composites via laser powder bed fusion and post-annealing. *J. Alloys Compd.* **2022**, *906*, 164288. [[CrossRef](#)]
112. Kang, N.; Li, Y.; Lin, X.; Feng, E.; Huang, W. Microstructure and tensile properties of Ti–Mo alloys manufactured via using laser powder bed fusion. *J. Alloys Compd.* **2019**, *771*, 877–884. [[CrossRef](#)]
113. Du, J.; Yang, Y.; Ren, Y.; Wu, H.; Shan, Q.; Wu, X.; Lu, Y.; Baker, I. A crack-free Ti-modified Al–Cu alloy processed by in-situ alloying laser powder bed fusion: Tribological behaviors and mechanical properties. *J. Alloys Compd.* **2023**, *960*, 170549. [[CrossRef](#)]
114. Ju, J.; Zan, R.; Shen, Z.; Wang, C.; Peng, P.; Wang, J.; Sun, B.; Xiao, B.; Li, Q.; Liu, S. Remarkable bioactivity, bio-tribological, antibacterial, and anti-corrosion properties in a Ti-6Al-4V-xCu alloy by laser powder bed fusion for superior biomedical implant applications. *Chem. Eng. J.* **2023**, *471*, 144656. [[CrossRef](#)]
115. Ravnkar, D.; Dahotre, N.B.; Grum, J. Laser coating of aluminum alloy EN AW 6082-T651 with TiB₂ and TiC: Microstructure and mechanical properties. *Appl. Surf. Sci.* **2013**, *282*, 914–922. [[CrossRef](#)]
116. Maurya, H.; Kosiba, K.; Juhani, K.; Sergejev, F.; Prashanth, K. Effect of powder bed preheating on the crack formation and microstructure in ceramic matrix composites fabricated by laser powder-bed fusion process. *Addit. Manuf.* **2022**, *58*, 103013. [[CrossRef](#)]
117. Parsons, E.M.; Shaik, S.Z. Additive manufacturing of aluminum metal matrix composites: Mechanical alloying of composite powders and single track consolidation with laser powder bed fusion. *Addit. Manuf.* **2022**, *50*, 102450. [[CrossRef](#)]
118. Tan, C.; Ma, W.; Deng, C.; Zhang, D.; Zhou, K. Additive manufacturing SiC-reinforced maraging steel: Parameter optimisation, microstructure and properties. *Adv. Powder Mater.* **2023**, *2*, 100076. [[CrossRef](#)]
119. Zhao, M.; Song, J.; Tang, Q.; Zhang, Z.; Feng, Q.; Han, Q.; Nie, Y.; Jin, P.; Jin, M.; Wu, H. Laser powder bed fusion of Inconel 718-based composites: Effect of TiB₂ content on microstructure and mechanical performance. *Opt. Laser Technol.* **2023**, *167*, 109596. [[CrossRef](#)]
120. Bai, P.; Huo, P.; Zhao, Z.; Du, W.; Zhang, Z.; Wang, L. Microstructure evolution and corrosion mechanism of in situ synthesized TiC/TC4 alloy nanocomposites fabricated by laser powder bed fusion. *Ceram. Int.* **2023**, *49*, 2752–2764. [[CrossRef](#)]
121. Wang, R.; Gu, D.; Huang, G.; Shi, K.; Yuan, L.; Zhang, H. Multilayered gradient titanium-matrix composites fabricated by multi-material laser powder bed fusion using metallized ceramic: Forming characteristics, microstructure evolution, and multifunctional properties. *Addit. Manuf.* **2023**, *62*, 103407. [[CrossRef](#)]
122. Melek, G.; Eloi, P.; Blandin, J.-J.; Pascal, C.; Donnadieu, P.; De Geuser, F.; Lhuissier, P.; Desrayaud, C.; Martin, G. Optimization of the strength vs. conductivity trade-off in an aluminium alloy designed for laser powder bed fusion. *Mater. Sci. Eng. A* **2022**, *858*, 144139.
123. Li, S.; Wang, X.; Le, J.; Han, Y.; Zong, N.; Wei, Z.; Huang, G.; Lu, W. Towards high strengthening efficiency by in-situ planting nano-TiB networks into titanium matrix composites. *Compos. Part B Eng.* **2022**, *245*, 110169. [[CrossRef](#)]
124. Li, L.; Wang, J.; Lin, P.; Liu, H. Microstructure and mechanical properties of functionally graded TiCp/Ti6Al4V composite fabricated by laser melting deposition. *Ceram. Int.* **2017**, *43*, 16638–16651. [[CrossRef](#)]
125. Rosito, M.; Vanzetti, M.; Padovano, E.; Gili, F.; Sampieri, R.; Bondioli, F.; Badini, C.F. Processability of A6061 Aluminum Alloy Using Laser Powder Bed Fusion by In Situ Synthesis of Grain Refiners. *Metals* **2023**, *13*, 1128. [[CrossRef](#)]
126. Deirmina, F.; AlMangour, B.; Grzesiak, D.; Pellizzari, M. H13–partially stabilized zirconia nanocomposites fabricated by high-energy mechanical milling and selective laser melting. *Mater. Des.* **2018**, *146*, 286–297. [[CrossRef](#)]
127. Bacon, D.; Edwards, L.; Moffatt, J.; Fitzpatrick, M.E. Fatigue and fracture of a 316 stainless steel metal matrix composite reinforced with 25% titanium diboride. *Int. J. Fatigue* **2013**, *48*, 39–47. [[CrossRef](#)]
128. Pagounis, E.; Talvitie, M.; Lindroos, V. Microstructure and mechanical properties of hot work tool steel matrix composites produced by hot isostatic pressing. *Powder Metall.* **1997**, *40*, 55–61. [[CrossRef](#)]
129. Hussain, M.; Mandal, V.; Kumar, V.; Das, A.; Ghosh, S. Development of TiN particulates reinforced SS316 based metal matrix composite by direct metal laser sintering technique and its characterization. *Opt. Laser Technol.* **2017**, *97*, 46–59. [[CrossRef](#)]
130. Wu, X.; Zhang, D.; Yi, D.; Hu, S.; Huang, G.; Poprawe, R.; Schleifenbaum, J.H. Interfacial characterization and reaction mechanism of Ti/Al multi-material structure during laser powder bed fusion process. *Mater. Charact.* **2022**, *192*, 112195. [[CrossRef](#)]
131. Belevi, F.; Casati, R.; Larini, F.; Riccio, M.; Vedani, M. Investigation on two Ti–B-reinforced Al alloys for laser powder bed fusion. *Mater. Sci. Eng. A* **2021**, *808*, 140944. [[CrossRef](#)]
132. Bhatnagar, S.; Mullick, S. A study on the influence of reinforcement particle size in laser cladding of TiC/Inconel 625 metal matrix composite. *Opt. Laser Technol.* **2023**, *161*, 109115. [[CrossRef](#)]

133. Wang, G.; Zhang, Y.; Zou, B.; Liu, Y.; Zheng, S.; Li, X.; Yan, W.; Li, Z.; Wang, Y.M. Enhanced plasticity due to melt pool flow induced uniform dispersion of reinforcing particles in additively manufactured metallic composites. *Int. J. Plast.* **2023**, *164*, 103591. [[CrossRef](#)]
134. Pan, C.; Zhu, D.; Luo, H.; Kosiba, K.; Qu, S.; Yang, C.; Li, X. Fabrication of high-performance CoCrNi medium entropy alloy by laser powder bed fusion: The effect of grain boundary segregation. *Compos. Part B Eng.* **2023**, *253*, 110540. [[CrossRef](#)]
135. Chen, Z.; Wen, X.; Wang, W.; Lin, X.; Yang, H.; Jiang, Z.; Chen, L.; Wu, H.; Li, W.; Li, N. Engineering fine grains, dislocations and precipitates for enhancing the strength of TiB₂-modified CoCrFeMnNi high-entropy alloy using Laser Powder Bed Fusion. *J. Mater. Res. Technol.* **2023**, *26*, 1198–1213. [[CrossRef](#)]
136. Zhao, C.; Deng, H.; Wang, Z. Microstructure and strength-ductility synergy of carbon nanotubes reinforced Mn–Cu alloy composites via laser powder bed fusion. *Mater. Sci. Eng. A* **2023**, *865*, 144658. [[CrossRef](#)]
137. Jiang, F.; Tang, L.; Li, S.; Ye, H.; Attallah, M.M.; Yang, Z. Achieving strength-ductility balance in a laser powder bed fusion fabricated TiB₂/Al–Cu–Mg–Ag alloy. *J. Alloys Compd.* **2023**, *945*, 169311. [[CrossRef](#)]
138. Mandal, V.; Tripathi, P.; Sharma, S.; Jayabalan, B.; Mukherjee, S.; Singh, S.S.; Ramkumar, J. Fabrication of ex-situ TiN reinforced IN718 composites using laser powder bed fusion (L-PBF): Experimental characterization and high-fidelity numerical simulations. *Ceram. Int.* **2023**, *49*, 14408–14425. [[CrossRef](#)]
139. Li, W.; Meng, L.; Wang, S.; Zhang, H.; Niu, X.; Lu, H. Plastic deformation behavior and strengthening mechanism of SLM 316L reinforced by micro-TiC particles. *Mater. Sci. Eng. A* **2023**, *884*, 145557. [[CrossRef](#)]
140. Zhou, Z.; Liu, Y.; Liu, X.; Wu, L. High-temperature tensile and creep properties of TiB-reinforced Ti6Al4V composite fabricated by laser powder bed fusion. *Mater. Charact.* **2023**, *200*, 112859. [[CrossRef](#)]
141. Li, X.; Li, G.; Zhang, M.-X.; Zhu, Q. Novel approach to additively manufacture high-strength Al alloys by laser powder bed fusion through addition of hybrid grain refiners. *Addit. Manuf.* **2021**, *48*, 102400. [[CrossRef](#)]
142. Sun, M.; Yang, Z.; Zhang, J.; Zhang, S.; Yang, Q.; Song, S.; Lu, B. Effects of ZrO₂ nanoparticles on the microstructure and mechanical properties of ZrO₂/AlSi10Mg composites manufactured by laser powder bed fusion. *Ceram. Int.* **2023**, *49*, 19673–19681. [[CrossRef](#)]
143. Kang, N.; Zhang, Y.; El Mansori, M.; Lin, X. Laser powder bed fusion of a novel high strength quasicrystalline Al–Fe–Cr reinforced Al matrix composite. *Adv. Powder Mater.* **2023**, *2*, 100108.
144. Cerit, A.A.; Karamis, B.M.; Fehmi, N.; Kemal, Y. Effect of reinforcement particle size and volume fraction on wear behavior of metal matrix composites. *Tribol. Ind.* **2008**, *30*, 31.
145. Ochiai, S.; Osamura, K. Influences of matrix ductility, interfacial bonding strength, and fiber volume fraction on tensile strength of unidirectional metal matrix composite. *Metall. Trans. A* **1990**, *21*, 971–977.
146. Ferguson, J.; Sheykh-Jaberi, F.; Kim, C.-S.; Rohatgi, P.K.; Cho, K. On the strength and strain to failure in particle-reinforced magnesium metal-matrix nanocomposites (Mg MMNCs). *Mater. Sci. Eng. A* **2012**, *558*, 193–204.
147. Boostani, A.F.; Tahamtan, S.; Jiang, Z.; Wei, D.; Yazdani, S.; Khosroshahi, R.A.; Mousavian, R.T.; Xu, J.; Zhang, X.; Gong, D. Enhanced tensile properties of aluminium matrix composites reinforced with graphene encapsulated SiC nanoparticles. *Compos. Part A Appl. Sci. Manuf.* **2015**, *68*, 155–163.
148. Li, Y.; Ramesh, K. Influence of particle volume fraction, shape, and aspect ratio on the behavior of particle-reinforced metal–matrix composites at high rates of strain. *Acta Mater.* **1998**, *46*, 5633–5646.
149. Narasimharaju, S.R.; Zeng, W.; See, T.L.; Zhu, Z.; Scott, P.; Jiang, X.; Lou, S. A comprehensive review on laser powder bed fusion of steels: Processing, microstructure, defects and control methods, mechanical properties, current challenges and future trends. *J. Manuf. Process.* **2022**, *75*, 375–414.
150. Vukkum, V.; Gupta, R. Review on corrosion performance of laser powder-bed fusion printed 316L stainless steel: Effect of processing parameters, manufacturing defects, post-processing, feedstock, and microstructure. *Mater. Des.* **2022**, *221*, 110874.
151. Hu, Z.; Zhu, H.; Zhang, H.; Zeng, X. Experimental investigation on selective laser melting of 17-4PH stainless steel. *Opt. Laser Technol.* **2017**, *87*, 17–25.
152. Tang, M.; Pistorius, P.C.; Beuth, J.L. Prediction of lack-of-fusion porosity for powder bed fusion. *Addit. Manuf.* **2017**, *14*, 39–48.
153. Douglas, R.; Lancaster, R.; Jones, T.; Barnard, N.; Adams, J. The Influence of Powder Reuse on the Properties of Laser Powder Bed-Fused Stainless Steel 316L: A Review. *Adv. Eng. Mater.* **2022**, *24*, 2200596. [[CrossRef](#)]
154. Cordova, L.; Bor, T.; de Smit, M.; Campos, M.; Tinga, T. Measuring the spreadability of pre-treated and moisturized powders for laser powder bed fusion. *Addit. Manuf.* **2020**, *32*, 101082. [[CrossRef](#)]
155. Popov, V.V., Jr.; Katz-Demyanetz, A.; Garkun, A.; Bamberger, M. The effect of powder recycling on the mechanical properties and microstructure of electron beam melted Ti-6Al-4 V specimens. *Addit. Manuf.* **2018**, *22*, 834–843. [[CrossRef](#)]
156. Ahmed, F.; Ali, U.; Sarker, D.; Marzbanrad, E.; Choi, K.; Mahmoodkhani, Y.; Toyserkani, E. Study of powder recycling and its effect on printed parts during laser powder-bed fusion of 17-4 PH stainless steel. *J. Mater. Process. Technol.* **2020**, *278*, 116522. [[CrossRef](#)]
157. Cordova, L.; Bor, T.; de Smit, M.; Carmignato, S.; Campos, M.; Tinga, T. Effects of powder reuse on the microstructure and mechanical behaviour of Al–Mg–Sc–Zr alloy processed by laser powder bed fusion (LPBF). *Addit. Manuf.* **2020**, *36*, 101625. [[CrossRef](#)]
158. Sutton, A.T.; Kriewall, C.S.; Karnati, S.; Leu, M.C.; Newkirk, J.W. Characterization of AISI 304L stainless steel powder recycled in the laser powder-bed fusion process. *Addit. Manuf.* **2020**, *32*, 100981. [[CrossRef](#)]

159. Young, Z.A.; Guo, Q.; Parab, N.D.; Zhao, C.; Qu, M.; Escano, L.I.; Fezzaa, K.; Everhart, W.; Sun, T.; Chen, L. Types of spatter and their features and formation mechanisms in laser powder bed fusion additive manufacturing process. *Addit. Manuf.* **2020**, *36*, 101438. [[CrossRef](#)]
160. Sutton, A.T.; Kriewall, C.S.; Leu, M.C.; Newkirk, J.W.; Brown, B. Characterization of laser spatter and condensate generated during the selective laser melting of 304L stainless steel powder. *Addit. Manuf.* **2020**, *31*, 100904. [[CrossRef](#)]
161. Kim, T.K.; Kim, M.-K.; Fang, Y.; Suhr, J. Moisture Effects on Qualities and Properties of Laser Powder Bed Fusion (LPBF) Additive Manufacturing of As-Built 17-4PH Stainless Steel Parts. *Metals* **2023**, *13*, 1550. [[CrossRef](#)]
162. Hovig, E.W.; Holm, H.D.; Sørby, K. *Effect of Processing Parameters on the Relative Density of AlSi10Mg Processed by Laser Powder Bed Fusion*; Advanced Manufacturing and Automation VIII 8; Springer: Berlin/Heidelberg, Germany, 2019; pp. 268–276.
163. Grubbs, J.; Sousa, B.C.; Cote, D. Exploration of the effects of metallic powder handling and storage conditions on flowability and moisture content for additive manufacturing applications. *Metals* **2022**, *12*, 603. [[CrossRef](#)]
164. Bidare, P.; Bitharas, I.; Ward, R.; Attallah, M.M.; Moore, A.J. Laser powder bed fusion in high-pressure atmospheres. *Int. J. Adv. Manuf. Technol.* **2018**, *99*, 543–555. [[CrossRef](#)]
165. Liu, J.; Wen, P. Metal vaporization and its influence during laser powder bed fusion process. *Mater. Des.* **2022**, *215*, 110505. [[CrossRef](#)]
166. Wang, X.; Zhang, L.; Fang, M.; Sercombe, T.B. The effect of atmosphere on the structure and properties of a selective laser melted Al–12Si alloy. *Mater. Sci. Eng. A* **2014**, *597*, 370–375. [[CrossRef](#)]
167. Zhao, D.; Yang, Q.; Wang, D.; Yan, M.; Wang, P.; Jiang, M.; Liu, C.; Diao, D.; Lao, C.; Chen, Z. Ordered nitrogen complexes overcoming strength–ductility trade-off in an additively manufactured high-entropy alloy. *Virtual Phys. Prototyp.* **2020**, *15* (Suppl. 1), 532–542. [[CrossRef](#)]
168. Xiao, Y.; Yang, Y.; Wu, S.; Chen, J.; Wang, D.; Song, C. Microstructure and mechanical properties of AlSi10Mg alloy manufactured by laser powder bed fusion under nitrogen and argon atmosphere. *Acta Metall. Sin. Engl. Lett.* **2022**, *35*, 486–500. [[CrossRef](#)]
169. Amano, H.; Ishimoto, T.; Suganuma, R.; Aiba, K.; Sun, S.-H.; Ozasa, R.; Nakano, T. Effect of a helium gas atmosphere on the mechanical properties of Ti-6Al-4V alloy built with laser powder bed fusion: A comparative study with argon gas. *Addit. Manuf.* **2021**, *48*, 102444. [[CrossRef](#)]
170. Traore, S.; Koutiri, I.; Schneider, M.; Lefebvre, P.; Rodrigues, J.; Dupuy, C.; Coste, F.; Peyre, P. Influence of gaseous environment on the properties of Inconel 625 L-PBF parts. *J. Manuf. Process.* **2022**, *84*, 1492–1506. [[CrossRef](#)]
171. Jacob, G.; Jacob, G. *Prediction of Solidification Phases in Cr-Ni Stainless Steel Alloys Manufactured by Laser Based Powder Bed Fusion Process*; US Department of Commerce, National Institute of Standards and Technology: Gaithersburg, MD, USA, 2018.
172. Cheng, B.; Wei, F.; Teh, W.H.; Lee, J.J.; Meng, T.L.; Lau, K.B.; Chew, L.T.; Zhang, Z.; Cheong, K.H.; Ng, C.K. Ambient pressure fabrication of Ni-free high nitrogen austenitic stainless steel using laser powder bed fusion method. *Addit. Manuf.* **2022**, *55*, 102810. [[CrossRef](#)]
173. Li, H.; Han, Y.; Feng, H.; Zhou, G.; Jiang, Z.; Cai, M.; Li, Y.; Huang, M. Enhanced strength-ductility synergy via high dislocation density-induced strain hardening in nitrogen interstitial CrMnFeCoNi high-entropy alloy. *J. Mater. Sci. Technol.* **2023**, *141*, 184–192. [[CrossRef](#)]
174. Qin, Y.; Liu, J.; Chen, Y.; Wen, P.; Zheng, Y.; Tian, Y.; Voshage, M.; Schleifenbaum, J.H. Influence of laser energy input and shielding gas flow on evaporation fume during laser powder bed fusion of Zn metal. *Materials* **2021**, *14*, 2677. [[CrossRef](#)]
175. Reijonen, J.; Revuelta, A.; Riipinen, T.; Ruusuvoori, K.; Puukko, P. On the effect of shielding gas flow on porosity and melt pool geometry in laser powder bed fusion additive manufacturing. *Addit. Manuf.* **2020**, *32*, 101030. [[CrossRef](#)]
176. Zhirnov, I.; Panahi, N.; Åsberg, M.; Krakhmalev, P. Process quality assessment with imaging and acoustic monitoring during Laser Powder Bed Fusion. *Procedia CIRP* **2022**, *111*, 363–367. [[CrossRef](#)]
177. Fang, Y.; Kim, M.-K.; Zhang, Y.; Duan, Z.; Yuan, Q.; Suhr, J. Particulate-reinforced iron-based metal matrix composites fabricated by selective laser melting: A systematic review. *J. Manuf. Process.* **2022**, *74*, 592–639. [[CrossRef](#)]
178. Qu, M.; Guo, Q.; Escano, L.I.; Nabaa, A.; Fezzaa, K.; Chen, L. Nanoparticle-enabled increase of energy efficiency during laser metal additive manufacturing. *Addit. Manuf.* **2022**, *60*, 103242. [[CrossRef](#)]
179. Nath, S.D.; Gupta, G.; Kearns, M.; Gulsoy, O.; Atre, S.V. Effects of layer thickness in laser-powder bed fusion of 420 stainless steel. *Rapid Prototyp. J.* **2020**, *26*, 1197–1208. [[CrossRef](#)]
180. Leicht, A.; Fischer, M.; Klement, U.; Nyborg, L.; Hryha, E. Increasing the productivity of laser powder bed fusion for stainless steel 316L through increased layer thickness. *J. Mater. Eng. Perform.* **2021**, *30*, 575–584. [[CrossRef](#)]
181. Thomas, M.; Baxter, G.J.; Todd, I. Normalised model-based processing diagrams for additive layer manufacture of engineering alloys. *Acta Mater.* **2016**, *108*, 26–35. [[CrossRef](#)]
182. Yang, K.-T.; Kim, M.-K.; Kim, T.; Kim, J.-H.; Suhr, J. Design optimization of smartphone camera housing fabricated by laser powder bed fusion using thermal analysis. *J. Mech. Sci. Technol.* **2022**, *36*, 699–708. [[CrossRef](#)]
183. Yang, K.-T.; Kim, M.-K.; Kim, D.; Suhr, J. Investigation of laser powder bed fusion manufacturing and post-processing for surface quality of as-built 17-4PH stainless steel. *Surf. Coat. Technol.* **2021**, *422*, 127492. [[CrossRef](#)]
184. Li, C.; Chen, Y.; Zhang, X.; Liu, T.; Peng, Y.; Wang, K. Effect of heat treatment on microstructure and mechanical properties of 17-4PH stainless steel manufactured by laser-powder bed fusion. *J. Mater. Res. Technol.* **2023**, *26*, 5707–5715. [[CrossRef](#)]
185. Fang, Y.; Kim, M.-K.; Zhang, Y.; Kim, T.; No, J.; Suhr, J. A new grain refinement route for duplex stainless steels: Micro-duplex stainless steel matrix composites processed by laser powder bed fusion. *Mater. Sci. Eng. A* **2023**, *881*, 145351. [[CrossRef](#)]

186. Wang, Z.; Li, H.; Shen, Q.; Liu, W.; Wang, Z. Nano-precipitates evolution and their effects on mechanical properties of 17-4 precipitation-hardening stainless steel. *Acta Mater.* **2018**, *156*, 158–171. [[CrossRef](#)]
187. Kang, N.; Li, Q.; El Mansori, M.; Yao, B.; Ma, F.; Lin, X.; Liao, H. Laser Powder Bed Fusion Processing of Soft Magnetic Fe–Ni–Si Alloys: Effect of Hot Isostatic Pressing Treatment. *Chin. J. Mech. Eng. Addit. Manuf. Front.* **2022**, *1*, 100054. [[CrossRef](#)]
188. Fiocchi, J.; Tuissi, A.; Biffi, C. Heat treatment of aluminium alloys produced by laser powder bed fusion: A review. *Mater. Des.* **2021**, *204*, 109651. [[CrossRef](#)]
189. Lai, J.; Zhang, Z.; Chen, X.-G. Precipitation strengthening of Al–B4C metal matrix composites alloyed with Sc and Zr. *J. Alloys Compd.* **2013**, *552*, 227–235. [[CrossRef](#)]
190. Gao, C.; Wu, W.; Shi, J.; Xiao, Z.; Akbarzadeh, A.H. Simultaneous enhancement of strength, ductility, and hardness of TiN/AlSi10Mg nanocomposites via selective laser melting. *Addit. Manuf.* **2020**, *34*, 101378. [[CrossRef](#)]
191. Deng, K.; Shi, J.; Wang, C.; Wang, X.; Wu, Y.; Nie, K.; Wu, K. Microstructure and strengthening mechanism of bimodal size particle reinforced magnesium matrix composite. *Compos. Part A Appl. Sci. Manuf.* **2012**, *43*, 1280–1284. [[CrossRef](#)]
192. Wang, M.; Song, B.; Wei, Q.; Shi, Y. Improved mechanical properties of AlSi7Mg/nano-SiCp composites fabricated by selective laser melting. *J. Alloys Compd.* **2019**, *810*, 151926. [[CrossRef](#)]
193. Yao, B.; Li, Z.; Teng, B.; Liu, J. Laser powder bed fusion of granulation-sintering-deoxygenation WC/18Ni300 composites: Anisotropic microstructure characterization and wear properties. *Rapid Prototyp. J.* **2023**, *29*, 1240–1256. [[CrossRef](#)]
194. Fang, Y.; Zhang, Y.; Kim, M.-K.; Kim, H.-I.; No, J.; Duan, Z.; Yuan, Q.; Suhr, J. An austenite-rich composite of stainless steels with high strength and favorable ductility via selective laser melting of a powder mixture. *Mater. Sci. Eng. A* **2022**, *855*, 143891. [[CrossRef](#)]
195. Humphreys, F.J. Recrystallization mechanisms in two-phase alloys. *Met. Sci.* **1979**, *13*, 136–145. [[CrossRef](#)]
196. Gu, D.; Ma, C. In-situ formation of Ni₄Ti₃ precipitate and its effect on pseudoelasticity in selective laser melting additive manufactured NiTi-based composites. *Appl. Surf. Sci.* **2018**, *441*, 862–870. [[CrossRef](#)]
197. Zhao, X.; Gu, D.; Ma, C.; Xi, L.; Zhang, H. Microstructure characteristics and its formation mechanism of selective laser melting SiC reinforced Al-based composites. *Vacuum* **2019**, *160*, 189–196. [[CrossRef](#)]
198. Zheng, Y.; Liu, F.; Zhang, W.; Liu, F.; Huang, C.; Gao, J.; Li, Q. The microstructure evolution and precipitation behavior of TiB₂/Inconel 718 composites manufactured by selective laser melting. *J. Manuf. Process.* **2022**, *79*, 510–519. [[CrossRef](#)]
199. He, D.; Wang, H.; Huang, W.; Chen, X.; Lian, G.; Wang, Y. Microstructure and Mechanical Properties of LaB₆/Ti-6Al-4V Composites Fabricated by Selective Laser Melting. *Metals* **2023**, *13*, 264. [[CrossRef](#)]
200. Mishra, R.S.; Thapliyal, S. Design approaches for printability-performance synergy in Al alloys for laser-powder bed additive manufacturing. *Mater. Des.* **2021**, *204*, 109640. [[CrossRef](#)]
201. Martin, J.H.; Yahata, B.D.; Hundley, J.M.; Mayer, J.A.; Schaedler, T.A.; Pollock, T.M. 3D printing of high-strength aluminium alloys. *Nature* **2017**, *549*, 365–369. [[CrossRef](#)]
202. Qu, M.; Guo, Q.; Escano, L.I.; Nabaa, A.; Hojjatzadeh, S.M.H.; Young, Z.A.; Chen, L. Controlling process instability for defect lean metal additive manufacturing. *Nat. Commun.* **2022**, *13*, 1079. [[CrossRef](#)]
203. Rees, D.T.; Leung, C.L.A.; Elambasseril, J.; Marussi, S.; Shah, S.; Marathe, S.; Brandt, M.; Easton, M.; Lee, P.D. In situ X-ray imaging of hot cracking and porosity during LPBF of Al-2139 with TiB₂ additions and varied process parameters. *Mater. Des.* **2023**, *231*, 112031. [[CrossRef](#)]
204. Liu, X.; Liu, Y.; Zhou, Z.; Wang, K.; Zhan, Q.; Xiao, X. Grain refinement and crack inhibition of selective laser melted AA2024 aluminum alloy via inoculation with TiC–TiH₂. *Mater. Sci. Eng. A* **2021**, *813*, 141171. [[CrossRef](#)]
205. Han, Q.; Gu, Y.; Huang, J.; Wang, L.; Low, K.W.Q.; Feng, Q.; Yin, Y.; Setchi, R. Selective laser melting of Hastelloy X nanocomposite: Effects of TiC reinforcement on crack elimination and strength improvement. *Compos. Part B Eng.* **2020**, *202*, 108442. [[CrossRef](#)]
206. Pan, C.; Li, X.; Luo, H.; Kosiba, K.; Qu, S.; Yang, C.; Zhu, D.; Zhang, C. Tuning the strength and ductility balance of a Co₃₂Cr₃₆Ni₃₂ medium entropy alloy fabricated by selective laser melting: Effect of segregations along grain boundaries. *Mater. Sci. Eng. A* **2022**, *840*, 142923. [[CrossRef](#)]
207. Guo, C.; Yu, Z.; Hu, X.; Li, G.; Zhou, F.; Xu, Z.; Han, S.; Zhou, Y.; Ward, R.M.; Zhu, Q. Y₂O₃ nanoparticles decorated IN738LC superalloy manufactured by laser powder bed fusion: Cracking inhibition, microstructures and mechanical properties. *Compos. Part B Eng.* **2022**, *230*, 109555. [[CrossRef](#)]
208. AlMangour, B.; Kim, Y.-K.; Grzesiak, D.; Lee, K.-A. Novel TiB₂-reinforced 316L stainless steel nanocomposites with excellent room- and high-temperature yield strength developed by additive manufacturing. *Compos. Part B Eng.* **2019**, *156*, 51–63. [[CrossRef](#)]
209. Chen, H.; Lu, T.; Wang, Y.; Liu, Y.; Shi, T.; Prashanth, K.G.; Kosiba, K. Laser additive manufacturing of nano-TiC particles reinforced CoCrFeMnNi high-entropy alloy matrix composites with high strength and ductility. *Mater. Sci. Eng. A* **2022**, *833*, 142512. [[CrossRef](#)]
210. Higashi, M.; Ozaki, T. Selective laser melting of pure molybdenum: Evolution of defect and crystallographic texture with process parameters. *Mater. Des.* **2020**, *191*, 108588. [[CrossRef](#)]
211. Gu, D.; Wang, H.; Dai, D.; Yuan, P.; Meiners, W.; Poprawe, R. Rapid fabrication of Al-based bulk-form nanocomposites with novel reinforcement and enhanced performance by selective laser melting. *Scr. Mater.* **2015**, *96*, 25–28. [[CrossRef](#)]
212. AlMangour, B.; Baek, M.-S.; Grzesiak, D.; Lee, K.-A. Strengthening of stainless steel by titanium carbide addition and grain refinement during selective laser melting. *Mater. Sci. Eng. A* **2018**, *712*, 812–818. [[CrossRef](#)]

213. AlMangour, B.; Grzesiak, D.; Yang, J.-M. Rapid fabrication of bulk-form TiB₂/316L stainless steel nanocomposites with novel reinforcement architecture and improved performance by selective laser melting. *J. Alloys Compd.* **2016**, *680*, 480–493. [[CrossRef](#)]
214. Zhu, Y.; Wu, X. Heterostructured materials. *Prog. Mater. Sci.* **2023**, *131*, 101019. [[CrossRef](#)]
215. Li, B.; Zhang, W.; Shen, J.; Xuan, F. Micro-laminated CoCrFeMnNi–TiNp/CoCrFeMnNi high-entropy alloy matrix composite with bimodal grain structure via multi-material selective laser melting (MM-SLM) additive manufacturing. *Compos. Commun.* **2022**, *36*, 101366. [[CrossRef](#)]
216. Yuan, F.; Yan, D.; Sun, J.; Zhou, L.; Zhu, Y.; Wu, X. Ductility by shear band delocalization in the nano-layer of gradient structure. *Mater. Res. Lett.* **2018**, *7*, 12–17. [[CrossRef](#)]
217. Zhu, Y.T.; Wu, X.L. Ductility and plasticity of nanostructured metals: Differences and issues. *Mater. Today Nano* **2018**, *2*, 15–20. [[CrossRef](#)]
218. Zhu, Y.; Wu, X. Perspective on hetero-deformation induced (HDI) hardening and back stress. *Mater. Res. Lett.* **2019**, *7*, 393–398. [[CrossRef](#)]
219. Nabarro, F.R.N.; Basinski, Z.S.; Holt, D.B. The plasticity of pure single crystals. *Adv. Phys.* **1964**, *13*, 193–323. [[CrossRef](#)]
220. Marattukalam, J.J.; Karlsson, D.; Pacheco, V.; Beran, P.; Wiklund, U.; Jansson, U.; Hjörvarsson, B.; Sahlberg, M. The effect of laser scanning strategies on texture, mechanical properties, and site-specific grain orientation in selective laser melted 316L SS. *Mater. Des.* **2020**, *193*, 108852. [[CrossRef](#)]
221. Malaki, M.; Xu, W.; Kasar, A.; Menezes, P.; Dieringa, H.; Varma, R.; Gupta, M. Advanced Metal Matrix Nanocomposites. *Metals* **2019**, *9*, 330. [[CrossRef](#)]

Disclaimer/Publisher’s Note: The statements, opinions and data contained in all publications are solely those of the individual author(s) and contributor(s) and not of MDPI and/or the editor(s). MDPI and/or the editor(s) disclaim responsibility for any injury to people or property resulting from any ideas, methods, instructions or products referred to in the content.